



Australian Government
Bureau of Meteorology

The Centre for Australian Weather and Climate Research
A partnership between CSIRO and the Bureau of Meteorology



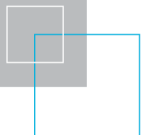
CAWCR Research Letters

Issue 10, July 2013

P. A. Sandery, T. Leeuwenburg, G. Wang, K. A. Day (editors)



www.cawcr.gov.au



ISSN: 1836-5949

Series: Research Letters (The Centre for Australian Weather and Climate Research); Issue 10.

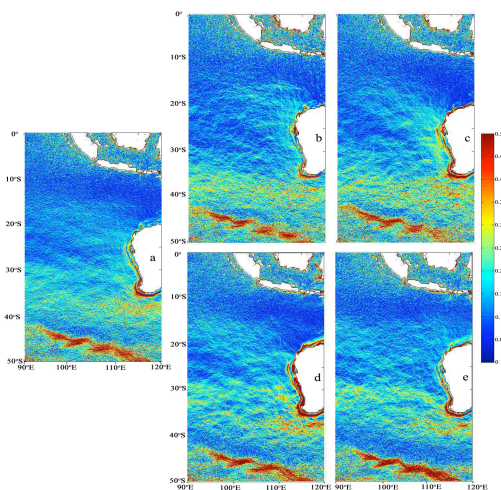
Copyright and Disclaimer

© 2013 CSIRO and the Bureau of Meteorology. To the extent permitted by law, all rights are reserved and no part of this publication covered by copyright may be reproduced or copied in any form or by any means except with the written permission of CSIRO and the Bureau of Meteorology.

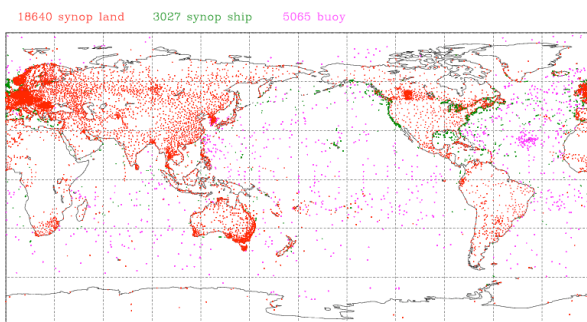
CSIRO and the Bureau of Meteorology advise that the information contained in this publication comprises general statements based on scientific research. The reader is advised and needs to be aware that such information may be incomplete or unable to be used in any specific situation. No reliance or actions must therefore be made on that information without seeking prior expert professional, scientific and technical advice. To the extent permitted by law, CSIRO and the Bureau of Meteorology (including each of its employees and consultants) excludes all liability to any person for any consequences, including but not limited to all losses, damages, costs, expenses and any other compensation, arising directly or indirectly from using this publication (in part or in whole) and any information or material contained in it.

Contents

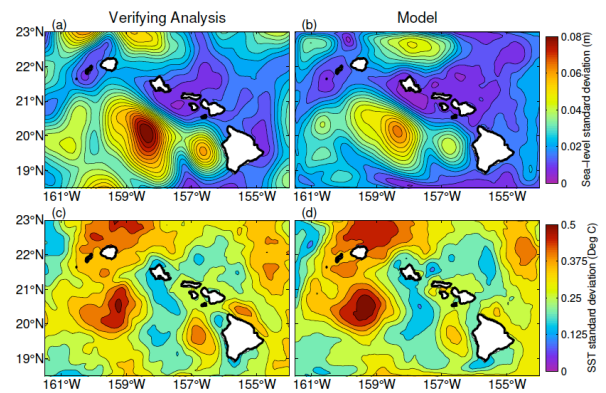
A High Resolution Sea Surface Temperature Climatology for the Southeast Indian Ocean	Prasanth Divakaran, Kenneth Casey, Gregg Foti, Gary Brassington, Deirdre Byrne	4
Determining the time of emergence of the climate change signal at regional scales	Les Muir, Jaclyn Brown, James Risbey, Susan Wijffels, Alex Sen Gupta	8
Constraining a regional ocean model with climatology and observations: Application to the Hawaiian Islands	Peter Oke, Madeleine Cahill, David Griffin, Mike Herzfeld	20
Impact of Satellite Observations on Southern Hemisphere Forecasts from the Operational ACCESS-G NWP Model	Jin Lee, John Le Marshall, Chris Tingwell, Belinda Roux	27
Vertical Structure and Diabatic Processes of the MJO, a Global Model Inter-comparison Project: preliminary results from the ACCESS model	Hongyan Zhu, Harry Hendon, Martin Dix, Zhian Sun, Gary Dietachmayer and Kamal Puri	34



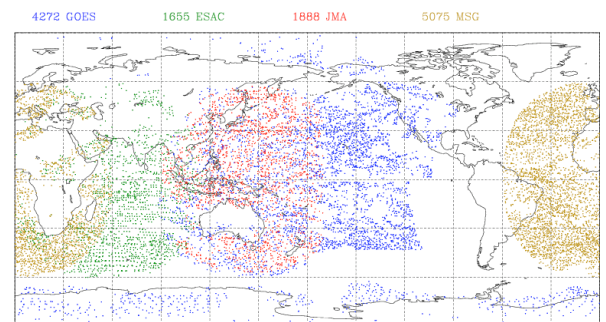
Australian BoM ACCESS-G Accepted observations coverage
Surface
20130610 0000 UTC
Total number of obs = 26732



Issue time 05UTC 10 Jun 2013



Australian BoM ACCESS-G Accepted observations coverage
Satwind
20130610 0000 UTC
Total number of obs = 12890



Issue time 05UTC 10 Jun 2013

Editors: P.A. Sandery, T. Leeuwenburg, G. Wang, K.A. Day
Enquiries: Dr Paul Sandery p.sandery@bom.gov.au
 CAWCR Research Letters
 The Centre for Australian Weather and Climate Research
 Bureau of Meteorology
 GPO Box 1298 Melbourne VICTORIA 3001

CAWCR Research Letters is an internal serial online publication aimed at communication of research carried out by CAWCR staff and their colleagues. It follows on from its predecessor *BMRC Research Letters*. Articles in *CAWCR Research Letters* are peer reviewed. For more information visit the *CAWCR* website.

A High Resolution Sea Surface Temperature Climatology for the Southeast Indian Ocean

Prasanth Divakaran^A, Kenneth S. Casey^B, Gregg Foti^B, Gary Brassington^A, Deirdre Byrne^B

^AThe Centre for Australian Weather and Climate Research

Bureau of Meteorology, Melbourne, Victoria

^BNOAA National Oceanographic Data Center, USA

p.divakaran@bom.gov.au

Introduction

Advanced Very High Resolution Radiometer (AVHRR) observations over the past 30 years, in combination with the Pathfinder Sea Surface Temperature algorithm provide long period high quality Pathfinder Sea Surface Temperature (SST) datasets. These datasets are known to be suitable for climate studies and climate change research (King and Greenstone, 1999). The latest in this range is the Pathfinder Version 5.2 dataset of global-scale SST fields at 4 km resolution for 1981-2010 (Casey et al., 2010). A by-product of this new data set is the construction of a high-resolution SST climatology. Examples of SST climatologies solely based on satellite data are the 9.28 km resolution global scale climatology by Casey and Cornillon (1999) and the regional high-resolution climatology for the North Atlantic by Mesias et al (2007).

In this study, we have developed daily climatologies of SST fields, at full resolution (4 km), using Pathfinder Version 5.2 data for 1993-2006, for the southeast Indian Ocean (SEIO) [90-120°E and 0-50°S]. Pathfinder Version 5.2 is an updated version of the Version 5.0 and 5.1 collection described by Casey et al. (2010). The weighted average approach to create climatologies from cloud contaminated datasets can produce isolated spike values in the mean fields. This is especially true in regions dominated by monsoon regimes (e.g., Tropical SEIO) as well as regions with persistent weather systems propagating through the mid-latitudes (e.g., Antarctic Circumpolar Current region of SEIO). To overcome these effects, we use a harmonic analysis method and novel techniques to fill data gaps, which are outlined below. The resulting algorithm leads to estimates that are more continuous both temporally and spatially. Such fields provide a more accurate reference field from which to derive SST anomalies.

Harmonic climatology method

A harmonic analysis of the time series data ‘the

harmonic climatology’ is created by applying a least square fit of the time series of SST data at each pixel to a cosine function containing both annual and semi-annual components:

$$SST_{c,lim} = A \cos\left(\frac{2\pi t}{T} + B\right) + C \cos\left(\frac{4\pi t}{T} + D\right) + E \quad (1)$$

where T is the annual period. The constants A and B correspond to the annual amplitude and annual phase, respectively. The constants C and D correspond to the semi-annual amplitude and phase. The constant E is the long term mean at that pixel.

The input time series consists of weekly (7-day) averages from daily mean fields Pathfinder version 5.2 best-quality data (quality flag 5) for 1993-2006. These data are archived by NODC in separate yearly accessions and are available online¹. To create a gap-free data set for analysis, a median spatial fill routine, with a box-size of 3 is applied to each 7-day SST average. Any remaining gaps in the weekly time series are filled by a temporal 1-dimensional Piecewise Cubic Hermite Interpolating Polynomial (PCHIP) function. A least square function is then fit to the SST time series and the five harmonic constants are calculated. Note: If fewer than 50 good observations are available for a given pixel, the amplitudes (A and C) are set to zero, phases (B and D) set to one, and the long term mean (E) is set to the mean at that pixel. In order to further improve the spatial continuity and further remove gaps, a spatial smoothing function is applied to the parameters. First, equation 1, is rewritten as

$$SST_{c,lim} = A \cos B \cos\left(\frac{2\pi t}{T}\right) - A \sin B \sin\left(\frac{2\pi t}{T}\right) + C \cos D \cos\left(\frac{4\pi t}{T}\right) - C \sin D \sin\left(\frac{4\pi t}{T}\right) + E \quad (2)$$

¹<http://data.nodc.noaa.gov/thredds/catalog/pathfinder/Version5.2/catalog.html>.

In this form the coefficients no longer have discontinuities relating to the periodicity in phase. A two dimensional spatial smoothing using a Hanning window of 0.25° half-width is applied to the coefficients $AcosB$, $AsinB$, $CcosD$ and $CsinD$ in equation 2. In this case, the coefficients are applied on a daily temporal-resolution to equation 2 to calculate sea surface temperature for any day in a climatological year.

Annual and seasonal climatology

The variability of the SEIO comprises a range of frequencies from mesoscale to interannual (Birol and Morrow 2001, Feng et al., 2005), due to the region being directly influenced by the seasonal monsoon winds and by remote forcing from the Indonesian Throughflow (ITF). The region is well known for the poleward flowing, eastern boundary, Leeuwin Current.

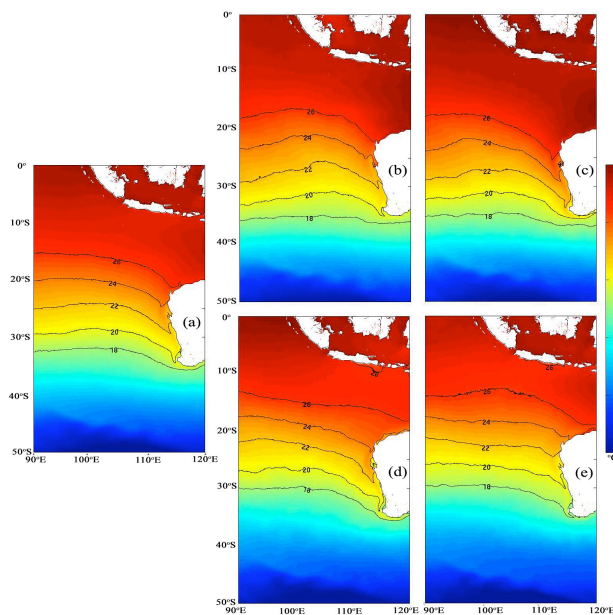


Figure 1 SST ($^{\circ}\text{C}$) for the annual mean (a) and seasonal means (b) DJF, (c) MAM, (d) JJA and (e) SON.

The Leeuwin Current transports relatively high SST water-masses from the tropics along the coast of Western Australia (Cresswell and Golding 1980). This is evident in the annual climatology as shown Figure 1a, as the approximate latitudinal isotherms over the ocean basin transition to a southward alignment adjacent to the west coast of Australia. The northward alignment of isotherms close to the coast supports the existence of an equatorward counter current along the coast (Taylor and Pearce, 1999; Pearce and Pattiaratchi, 1999).

In the harmonic climatology, the equatorward sloping isotherms during Austral spring, are seen northward of the previously reported Ningaloo Reef

extend. Eastward transports of warm water along the Great Australian Bight by the Leeuwin Current are also clearly seen in Figure 1a. The general characteristic meridional gradient from low to high latitudes is present over the open waters of the southeast Indian Ocean, with perturbations present in higher latitudes characteristic of the Antarctic circumpolar current. Isotherms east of $\sim 105^\circ\text{E}$ show southward slope towards the coast, analogous to those documented by Godfrey and Ridgway (1985; Figure 5) for steric height. Seasonal variations in open ocean SST are mainly a direct response to the amount of solar radiation into the sea surface. Such seasonal north-south oscillations of isotherms are evident in Figure 1b-e. The 18°C isotherm is seen much closer to 30°S during Austral winter and spring, than the other two seasons.

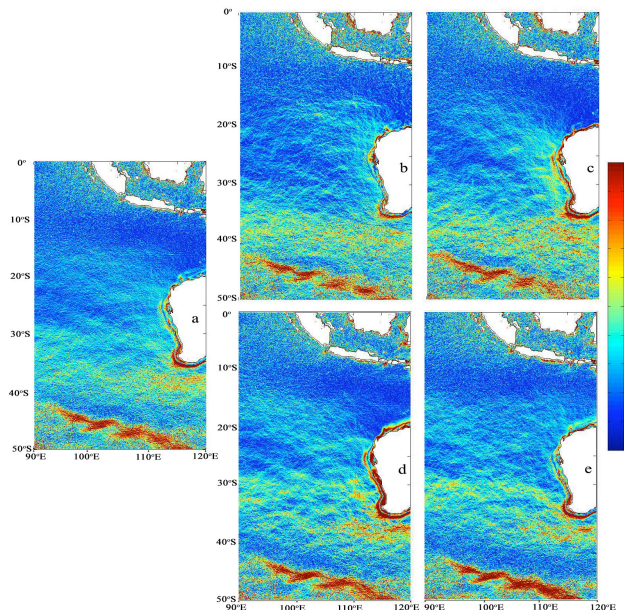


Figure 2 SST gradient ($^{\circ}\text{C}/\text{km}$) for the annual mean (a) and seasonal means (b) DJF, (c) MAM, (d) JJA and (e) SON.

The seasonal upwelling signatures off the coast of Java are clearly visible as a low SST patch during Austral Spring (Sasanto et al., 2001). The transport of heat by the Leeuwin Current strengthens in autumn and winter in line with the seasonal cycle of the volume transport (Feng et al., 2002). This has been clearly observed in harmonic climatology shown in Figure 1c-d, where the isotherm closest to Cape Leeuwin has been advected further eastward into the Great Australian Bight by the stronger Leeuwin Current transports. Evidence for a northward counter current along the inner shelf-edge is seen as a continuous cooler SST, with the exception of Austral winter.

SST Gradient Intercomparison

Gradient magnitude are computed from spatial differences using the central difference method; they are useful in showing how well different techniques can resolve coherent features as well as in highlighting isolated spike error values in the mean fields. Figure 2 shows the magnitude of SST gradient for annual and seasonal-mean constructed using the harmonic analysis method. Similarly, Figure 3 represents the same quantity for SST annual and seasonal maps constructed from cumulative averages.

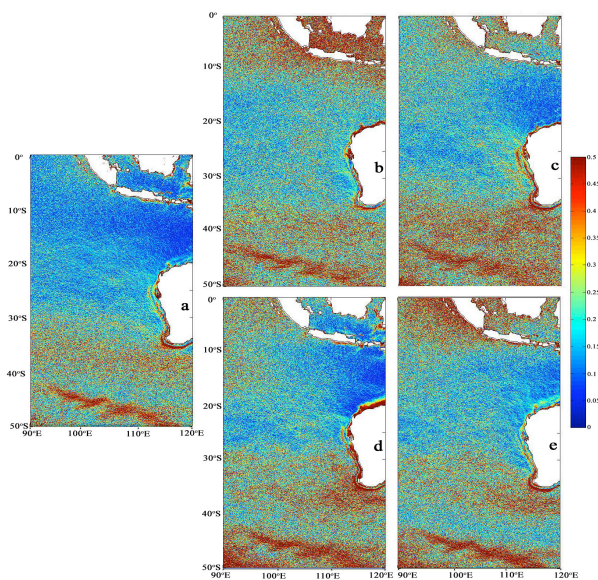


Figure 3 SST gradient ($^{\circ}\text{C}/\text{km}$) using cumulative average for the annual mean (a) and seasonal means (b) DJF, (c) MAM, (d) JJA and (e) SON.

For each corresponding plot shown in Figure 2 and Figure 3, the harmonic method shows greater continuity of features and a reduction in the grid scale noise. Figure 2 better captures the low SST gradient magnitudes on the northern-side of the Antarctic Front, which has been widely noted for its effect on boundary layer winds (O'Neill et al., 2003). Seasonal spatial gradients also capture the variability in strength and structure of the Leeuwin Current system, which are clearer in Figure 2 than in Figure 3. In general, there are clear improvements in harmonic climatology, compared with the weighted average method. This improvement is particularly evident in regions with significant cloud cover; such as the Indonesian region (affected by the summer monsoon) and the mid-latitudes (affected by the transient weather systems) of the southeast Indian Ocean. Figure 3, shows large values in SST gradient both in magnitude and its spatial extent, with less defined oceanographic features of the region. Both the above issues can be attributed to the fitting errors in the weighted average approach. The spatial

gradient maps constructed from the harmonic method are largely devoid of these problems. Magnitude and spatial extent of gradients get greater for the seasonal-mean plots in Figure 3. This can be attributed to the decrease in weighting owing to the smaller number of samples due to cloud cover and other factors that contaminate the satellite observations. Such problems can be effectively removed by the harmonic climatology method.

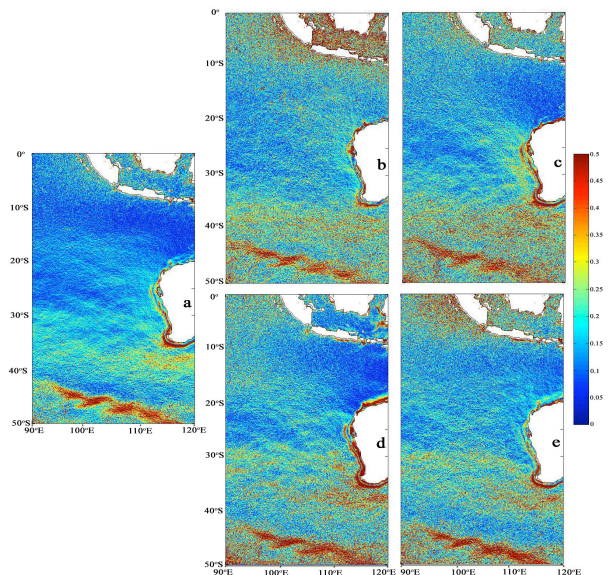


Figure 4 SST gradient ($^{\circ}\text{C}/\text{km}$) without coefficient smoothing for the annual mean (a) and seasonal means (b) DJF, (c) MAM, (d) JJA and (e) SON.

Conclusions

A new high-resolution SST climatology for the SEIO, from 14-years of Pathfinder AVHRR daily-mean fields has been presented. We note that the 14-year period is relatively short for the construction of climatologies, considering the 30-years of available Pathfinder data. In particular, we have chosen a period that corresponds to the period of satellite altimetry and planned further studies with Bluelink Reanalysis (BRAN 2.1), 1993-2006.

Regardless of the period of study, the new harmonic climatology shows great promise in showing coherent features and capturing seasonal variations. The study reveals the structure of the Leeuwin Current system in great detail, with its seasonality and influence of equatorward counter flows. The upwelling signatures off the coast of Java and the colder waters of the Antarctic front are also clearly represented. In summary, Harmonic analysis is able to do better reconstruct the climatology from cloud-contaminated fields. The use of continuity of the coefficients found as an effective method for

filling gaps and removing noise (see Figure 2 and Figure 4). This is particularly evident in regions with persistent cloud cover such as the tropical Indian Ocean and the mid-latitudes of the southeast Indian Ocean. This short study also inspires us to use all the available Pathfinder data in the future, and using the method described in this paper to construct climatologies for the global ocean, which can be used as a basis for constructing anomalies.

Acknowledgements

PD and GB acknowledge the support of BlueLink project. Acknowledgements also given to organizations and staffs that maintain NOAA satellites, and to the NODC AVHRR Pathfinder Data Program.

References

- Birol, F. and Morrow, R. A., 2001: Source of baroclinic waves in the southeast Indian Ocean. *Journal of Geophysical Research*, 106(C5), 9145-9160.
- Cresswell, G. R and Golding, T. J, 1980: Observation of a south-flowing current in the southeast Indian Ocean, *Deep Sea Research*, 27A, 449-466.
- Casey, K.S., Cornillon, P.C., 1999: A comparison of satellite and in situ based sea surface temperature climatologies. *Journal of Climate* 12, 1848-1863.
- Casey, K. S., T.B. Brandon, P. Cornillon, and R. Evans, 2010: The past, present and future of the AVHRR Pathfinder SST program. *Oceanography from Space: Revisited*, eds. V. Barale, J.F.R. Gower, and L. Alberotanza, Springer. DOI: 10.1007/978-90-481-8681-5_16.
- Feng, M., Li, Y, and Meyers, G, 2004: Multidecadal variations of fremantle seas level: Footprint of climate variability in the tropical Pacific. *Geophysical Research Letters*, 31(16), L16302.
- Feng, M., Meyers, G., Pearce, A. and Wijffels, S. E, 2003: Annual and interannual variations of the Leeuwin current at 32°S, *Journal of Geophysical Research*, 108(11), 3355, doi:10.1029/2002JC001763.
- Godfrey, J. S. and Ridgway, K. R, 1985: The large-scale environment of the poleward-flowing Leeuwin Current, Western Australia: longshore steric height gradients, wind-stresses and geostrophic flow, *Journal of Physical Oceanography*, 15, 481-495.
- King, M.D, Greenstone, R, eds, 1999: *Earth Observing System (EOS) Reference Handbook*. National Aeronautics and Space Administration, EOS Project Science Office, 355 pp.
- Mesias, J.M., J.J. Bisagni, and A.-M.E.G Brunner, 2007: A high-resolution satellite derived sea surface temperature climatology for the western North Atlantic Ocean. *Continental Shelf Research*, 27 (2), 191-207.
- O'Neill, L. W., D. B. Chelton, and Esbensen, S, K, 2003: Observations of SST-Induced Perturbations of the Wind Stress Field over the Southern Ocean on Seasonal Timescales, 16, 2340-2354.
- Pearce, A., and Pattiaratchi, C 1999: Capes Current: a summer counter-current flowing past Cape Leeuwin and Cape Naturaliste, Western Australia, *Continental Shelf Research*, 19, 401-420
- Susanto, R. D., A. L Gordon, and Zheng, Q, 2001: Upwelling along the coasts of Java and Sumatra and its relation to ENSO, *Geophysical Research Letters*, 28 (8), 1599-1602.
- Taylor, J. G., and Pearce, A. F, 1999: Ningaloo Reef currents: implication for coral spawn dispersal, zooplankton and whale shark abundance, *Journal of Royal Society of Western Australia*, 82, 57-65.

Determining the time of emergence of the climate change signal at regional scales

Les C. Muir^A, Jaclyn N. Brown^A, James S. Risbey^A, Susan E. Wijffels^A

and Alex Sen Gupta^B

^AThe Centre for Australian Weather and Climate Research, Hobart, Australia.

^BUniversity of New South Wales, Sydney, Australia

Introduction

Significant changes to our climate from increasing emissions of greenhouse gases and other anthropogenic drivers are becoming inevitable. However, limited observational records (both spatially and temporally) and imperfect climate models can hamper our ability to differentiate between changes that are attributable to greenhouse forcing outside of the natural climate variability. As such, particularly at regional or local scales, attributing long-term change to particular drivers is a challenge. Global coupled models can be used to help us to explore this question. In particular we can take advantage of long pre-industrial control simulations to determine a model's inherent natural variability and use this to understand at what time an externally forced signal can be clearly identified. Determining the spatial patterns of the 'time of emergence' of the climate change signal in models provides insights into where and when we might expect to see significant changes to the climate.

The spatial patterns of signal to noise have been investigated previously at large and regional scales (Barnett and Schlesinger 1987; Santer et al. 1995b). There has also been previous work determining a time at which the signal will be detectable at large-scales (Karl et al. 1991; Santer et al. 1995a). Recently there has been work that has focused on determining the time at which the anthropogenically forced signal is detectable at the regional level. (Kattsov and Sproyshev 2006; Mahlstein et al. 2011; Giorgi and Bi 2009; Hawkins and Sutton 2012; Mahlstein et al. 2012).

Kattsov and Sproyshev (2006) investigated the emergence of decadal atmospheric temperatures and found that the earliest emergence occurs in the tropical Indian Ocean and the Western Pacific. Both observations and models consistently suggested that the emergence of an anthropogenic signal has already occurred in the Indian Ocean and the Western Pacific. Conversely the latest emergence

was found to occur in the North Atlantic Ocean and the Southern Ocean in the mid 21st century.

Two recent studies have investigated the time at which changes to seasonal temperature will be detectable. Diffenbaugh and Scherer (2011) investigated the emergence time relative to the maximum seasonal temperature of the 20th century and found a spatial signature consistent with the emergence of decadal temperature signals. The earliest emergence for temperature extremes was found in the tropical Indian Ocean and the Western Pacific Ocean. Similarly, Mahlstein et al. (2011) investigated summer temperature changes and investigated the time of emergence with reference to a global mean temperature change. Again emergence was found earliest in the tropics, requiring between 0.2°C and 0.6°C global temperature change temperature change above 1900-1929 levels. Hawkins and Sutton (2012) looked at the emergence of near-surface air temperature for half-year seasons. They again found similar emergence times to the above studies that looked at seasonal temperature. However, they found considerable uncertainty in the emergence estimate as a result of inter-model spread in the signal of change, and the magnitude of internal variability. This resulted in up to 60 years difference in some regions.

Timing of the emergence of precipitation changes has also been examined. Giorgi and Bi (2009) investigated the timing of precipitation changes for 14 land locations around the globe. The earliest emergence was found to be in northern hemisphere high-latitudes, the Mediterranean and eastern Africa. India, China and the Caribbean were next to emerge, with the southern hemisphere subtropics and American west coast last. Mahlstein et al. (2012) investigated the emergence of wet season land precipitation changes with respect to the global mean temperature change. They found that a 1.4 °C global average temperature rise is required to first detect a robust wet season precipitation change.

Emergence would be first detectable in the Northern Hemisphere high latitudes with an increase in precipitation. There was found to be good agreement amongst the models on the direction of emergence, for those regions that emerged.

In this paper we investigate emergence times of decadal temperatures and precipitation, while most recent studies have investigated annual emergence. Emergence is determined as the time when the climate change signal exceeds the model's estimate of the decadal variability and remains above the threshold for the remainder of the perturbation experiment. As we will demonstrate, large meridional differences in the time of emergence is evident in the various properties examined. Consequently we begin our assessment on the spatial distribution of emergence by examining zonal decadal means of sea surface temperature, near-surface air temperature and precipitation. As there are also regional differences to these broad scale patterns we further investigate spatial maps of emergence on a 1° grid for sea surface temperature, near-surface air temperature and precipitation. Emergence times of SST and ocean Precipitation have not been calculated previously at the decadal time scale, nor has this calculation been made on zonal means of the above variables.

While large places on the planet may not see significant changes to annual precipitation until after 2100, decadal precipitation changes might be evident well before then. The timing of emergence at the decadal time scale can also be useful to a different user base than the annual time scale. We also consider global precipitation rather than just land precipitation.

Method

The time of emergence (TOE) for a particular model, variable and location is the year at which the time series from an anthropogenically forced signal simulation permanently exceeds the variability determined from the corresponding pre-industrial control simulation (picntrl, Figure 1). The models used in this study are from the CMIP3 model database (Table 1) (Meehl et al. 2007).

The forced simulation is constructed from the concatenation of a 20th century (20c3m) and 21st century (sresa1b) simulations (Figure 1). The 20th century and 21st century simulations include both anthropogenic and natural external forcings. All model output is first bi-linearly interpolated to a common 1° grid. The individual model input resolutions vary with atmospheric variables on from 1.12° x 1.12° to 4° x 5° and oceanic variables from 0.19° x 0.28° to 4° x 5°. A 10-year running mean is performed to investigate decadal time scales. At each

grid point a linear trend is calculated in the pre-industrial control simulation to obtain an estimate of model drift (Sen Gupta et al. 2011). This trend is subsequently removed from both the forced and unforced simulations.

Table 1 List of models used and the length of the pre-industrial control simulation used for the respective variables

	Model Name	SAT	SST	PRECIP
1	bccr_bcm2_0	250	250	250
2	cccma_cgcm3_1_t47	1001	1001	1001
3	cccma_cgcm3_1_t63	350	400	350
4	cnrm_cm3	500	500	500
5	csiro_mk3_0	380	500	380
6	csiro_mk3_5	330	480	1220
7	gfdl_cm2_0	500	500	500
8	gfdl_cm2_1	500	300	--
9	giss_aom	251	251	251
10	giss_model_e_h	400	400	400
11	giss_model_e_r	500	500	500
12	iap_fgoals	150	350	150
13	inm_cm3_0	330	330	330
14	ipsl_cm4	230	--	500
15	miroc3_2_hires	100	100	100
16	miroc3_2_medres	500	500	500
17	miub_echo_g	341	341	341
18	mpi_echam5	506	--	506
19	mri_cgcm2_3_2a	350	350	350
20	ncar_ccsm3_0	230	--	230
21	ukmo_hadcm3	341	341	341
22	ukmo_hadgem1	140	239	239
Total Models		22	19	21
Above 400 years		8	9	9

The 'emergence threshold' is calculated as three standard deviations from the detrended unforced pre-industrial control simulation for a particular variable and location, representing the size of the internal decadal and longer-term variability. The time of emergence is defined as the last year in which the decadal running mean anomaly from the forced simulation (relative to the mean of the pre-industrial control simulation) lies within the emergence threshold and then never returns. This represents a very strong condition on when the anthropogenically forced signal is clearly distinguishable from the background variability. This method is similar to the permanent exceedance method in Diffenbaugh and Scherer (2011) except that their threshold was the 20th century maximum annual temperature.

The variables investigated in this study are near-surface atmospheric temperature (SAT, 22 models), sea surface temperature (SST, 19 models) and precipitation (21 models). Model names and the lengths of the available controls simulations are found in Table 1. All of the models studied have more than 100 years of data in their pre-industrial control simulations. The future warming scenario, sresa1b, is chosen as it contains the greatest number of models for the variables considered. A single ensemble member is used for each model considered.

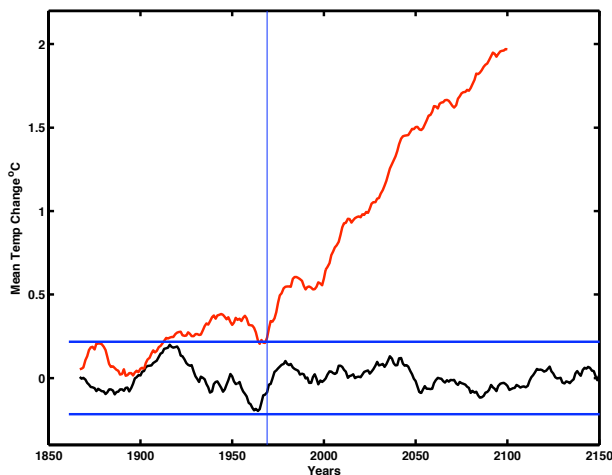


Figure 1 Example of the 'Time of Emergence' calculation. Time series shown are for 10 year running means of the unforced (black line) and the forced (red line) simulations. The three standard deviation envelope of variability is indicated by the horizontal blue line shows the time of emergence.

Results

Sea Surface Temperature

The TOE is dependent on both the magnitude of the forced change and the size of the variability at a given point. As such differing magnitudes of simulated decadal variability in climate models is an important consideration in determining the time of emergence. We first compare the observed decadal zonal mean sea surface temperature variability from the 141 year HADISST (Rayner et al. 2003) observations and the 155 year KAPLAN SST V2 observations (Kaplan et al. 1998) (Figure 2a) with the models output. As an unforced estimate of variability does not exist the observations have been detrended using a second order polynomial to remove a portion of the broad scale forced signal. Both observational data sets show the largest variability in the northern mid- to high-latitudes with lower variability in the tropics and subtropics. A localized peak in variability is found at the equator related to PDO/IPO variability.

The multi-model mean decadal variability in sea surface temperature is less than the observational estimates within the tropics, lying close to the maximum model estimates in variability. In the northern hemisphere mid-latitudes half of the models overestimate the variability dramatically. This overestimation comes predominately from simulated very high decadal variability in the northern Atlantic Ocean and was also found in interannual variability by Mahlstein et al. (2011). The localized peak in variability at the equator does not exist in 3 models, and is over pronounced in 6 models.

The pattern of the time of emergence for zonal mean SST is similar across almost all of the models, with the tropical and equatorial regions emerging first (Figure 3a) and the high and mid-latitudes emerging later. The reason for this pattern is a combination of both the decadal variability and the mean change. The tropics have large forced temperature changes with relatively small decadal variability, while relative to the tropics, at higher latitudes there is much larger decadal variability but a smaller forced change (Figure 3b).

The variability in the tropics lies close to the larger model estimates and the giss_model_e_h is one of these large estimates. The emergence for this model is the latest emergence in the tropics at 2011, which might be a better estimate of the actual emergence time rather than the multi-model median.

Four of the models show evidence of an emergence with a reduction of temperature in the high latitude region's of both hemispheres, while the models with the largest variability at high latitudes exhibit no emergence by 2100.

The largest spread in emergence times are at the high latitudes of both hemispheres with up to 170 years difference between the earliest and latest model emergences. This is due to large differences across the models in the climate signal and noise. Large spread in individual model emergence times was also found in Hawkins and Sutton (2012) while looking at seasonal atmospheric temperature.

Some of the models that do not emerge in the southern hemisphere (green pluses) have the largest variability at that latitude (e.g. csiro_mk3_0) while others with smaller variability do not emerge because the climate change signal is small (e.g. gfdl_cm2_1). In a CMIP3 intercomparison for the Southern Ocean, Sen Gupta et al. (2009) show that for many models there is no significant projected increase in SST over the 21st century as any additional heat going into the ocean is advected northwards in the surface layer.

There is good agreement in all of the models that the high-latitude regions will emerge later than the low-latitude regions even if the time frame of this emergence is not certain. The multi-model median emergence times (Figure 3) occur first within the subtropics around 1950 then the equator 10 years later and finally the high-latitudes last.

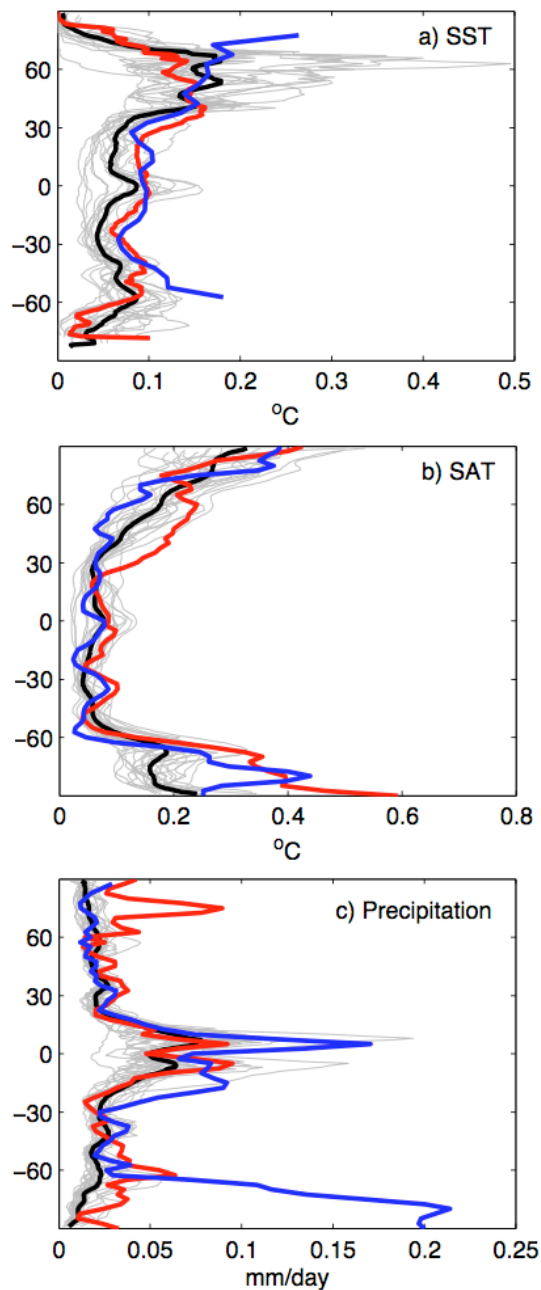


Figure 2 Standard deviation of the zonal decadal mean a) sea surface temperature b) surface atmospheric temperature and c) precipitation. Red and blue lines are the observational / reanalysis estimates a) HadISST (red) KAPLAN SST V2 (blue) b) ERA40 (red), NCEP2 (blue) c) GPCP (red) CMAP (blue). Grey lines are the individual model estimates. The black lines are the multi-model mean.

To examine regional differences in emergence times, spatial patterns of emergence times from the models are shown in Figure 4. In the tropical Pacific the equatorial cold tongue emerges later than the surrounding subtropics in a large number of models. This is despite the fact that the projected warming is simulated to be relatively strong in the equatorial central and eastern Pacific (Xie et al. 2010). This presumably stems from the peak in intrinsic variability associated with the ENSO and the PDO/IPO, identified in the zonally averaged

variability (Figure 2). The equatorial Indian Ocean and western Pacific Ocean are the regions of earliest emergence in all but two models and the zonal and meridional extent differs in all of the models.

Regions in the Southern Ocean and the Northern Atlantic Ocean do not emerge by 2100 in 17 and 14 models respectively. The spatial scale and position of this region is different in all of the models. The reason for this emergence is due to a combination of large decadal variability and a small forced signal. For most models and locations the emerging signal is one of warming, however for 8 models a cooling signal is evident in deep mixing regions around Greenland and the Southern Ocean.

There are inter-model differences in the emergence times and by taking a multi-model median we can identify those features that are robust across the models (Figure 5). In the Pacific Ocean the slightly later emergence noted above is apparent within the equatorial cold tongue compared to the rest of the tropical and subtropical regions.

The multi-model median suggests emergence of temperature in the tropics before the year 2000 and the mid- and high-latitude regions emerging by 2050. There are however locations in the northern Atlantic, southern Atlantic and Southern Ocean associated with the deep mixing regions where there is no agreement on if an emergence will occur or on the direction of emergence if it occurs. The maximum time of emergence outside of the equatorial Pacific cold tongue is 2025, while within the Indian Ocean the maximum is the year 2000, which might be better estimates of the time of emergence due to underestimates in variability.

Surface Atmospheric Temperature

Figure 2b shows the decadal variability estimates from both the 45 year ERA 40 reanalysis (Uppala et al. 2005) and the 30 year NCEP2 reanalysis (Kanamitsu et al. 2002). Linear detrending is used to remove a broad warming trend. Similar to SST, the lowest decadal variability of both reanalysis products is in the tropics and increases towards higher latitudes. The two observational data sets agree quite well in the zonal pattern of variability.

In general the models show a similar increase in decadal variability towards higher latitudes with the multi-model mean lying close to the observational estimates. Polewards of 50°S many models have considerably lower variability than the reanalysis products. Some models displaying half the variability of the observations. This could be due to the relatively short observational records, which will not adequately sample multi-decadal variability. Mahlstein et al. (2011) investigated interannual

variability rather than decadal and found large underestimates in variability, particularly over land.

The emergence for zonal mean SAT in Figure 3c is similar across all of the models. As for SST, the tropics and subtropics emerge first and the high and mid-latitudes emerge later. While the magnitude of

the change in temperature is largest at the high-latitudes (Figure 3d), the decadal variability at these latitudes is also high. The reverse occurs at the equator where the variability is small compared to the change in temperature, which results in an early emergence.

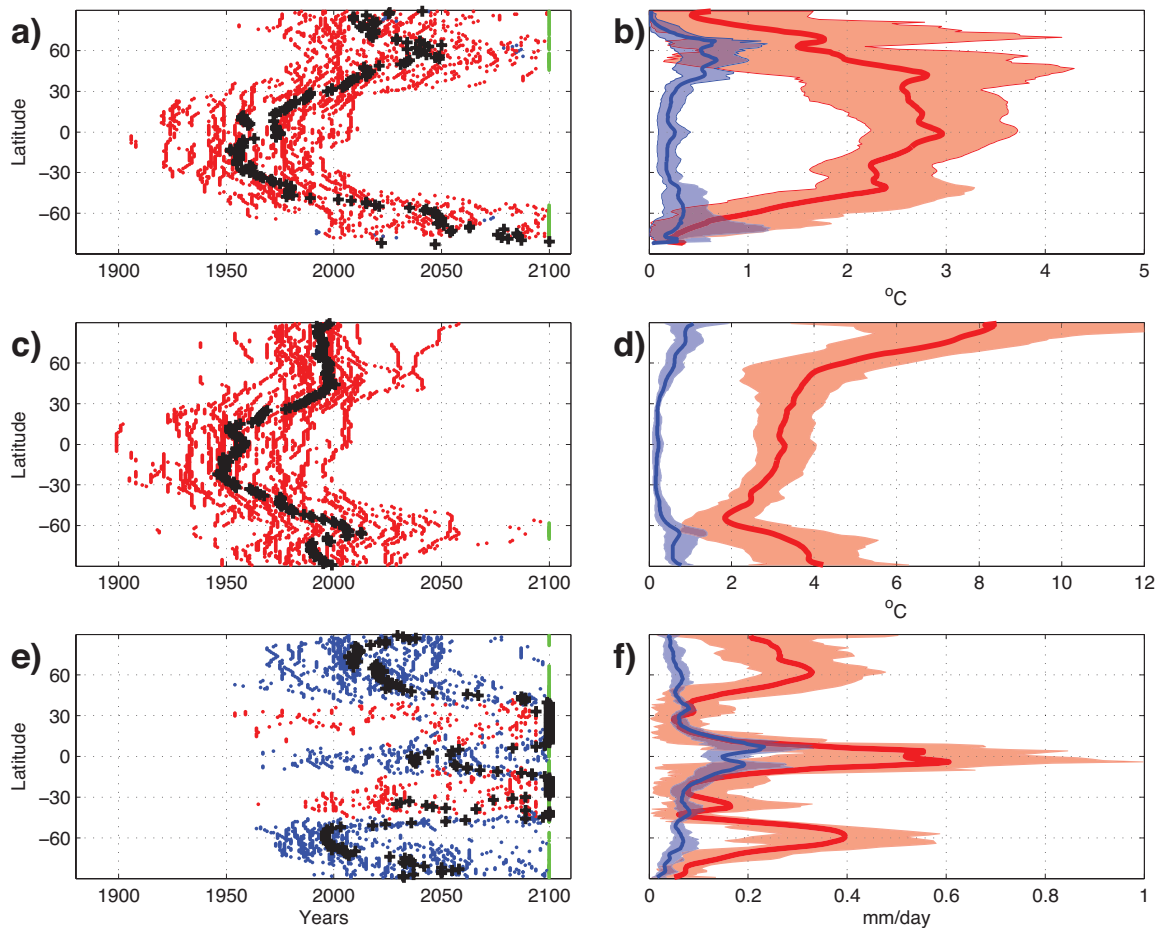


Figure 3 Time of Emergence of zonally averaged a) SST, c) SAT, e) Precipitation and zonal signal and zonal noise b) SST, d) SAT and f) Precipitation. For SAT (a) and TAS (c) red dots indicate an emergence with an increase in temperature, blue dots an emergence with a decrease in temperature. For precipitation (f) blue indicates an emergence with an increase in precipitation while red dots an emergence with a decrease in precipitation. Green dots indicate no emergence by 2100. Black crosses are the multi-model median emergence. (b, d and f) Multi-model mean zonal absolute change to 2090-2100, indicated by the red line with the 10th and 90th percentiles shaded light red and the multi-model mean emergence threshold, blue line and the 10th and 90th percentiles shaded light blue.

The multi-model median time of emergence in the tropics is 1950, while the mid-latitudes and poles mostly emerge before 2000. The latest median emergence on the planet is found at 60°S in the year 2100. The difference between the earliest and latest times of emergence is approximately 100 years at all latitudes.

The median emergence in SAT occurs 10 years before SST in the tropics and up to 60 years earlier in the mid-latitudes. The southern hemisphere high latitudes emerge in SAT 100 years before SST while

the northern hemisphere approximately 50 years. The spatial pattern of multi-model median emergence is shown in Figure 6. South of Greenland and north of the Ross Sea in the Southern Ocean are the only regions where there is less than two-thirds model agreement on if emergence will occur or on the direction of emergence by 2100. These regions are also where the models do not agree on emergence for SST. The multi-model median and individual model emergence times are very similar to the multi-model mean emergence found in Kattsov and Sproyshev (2006).

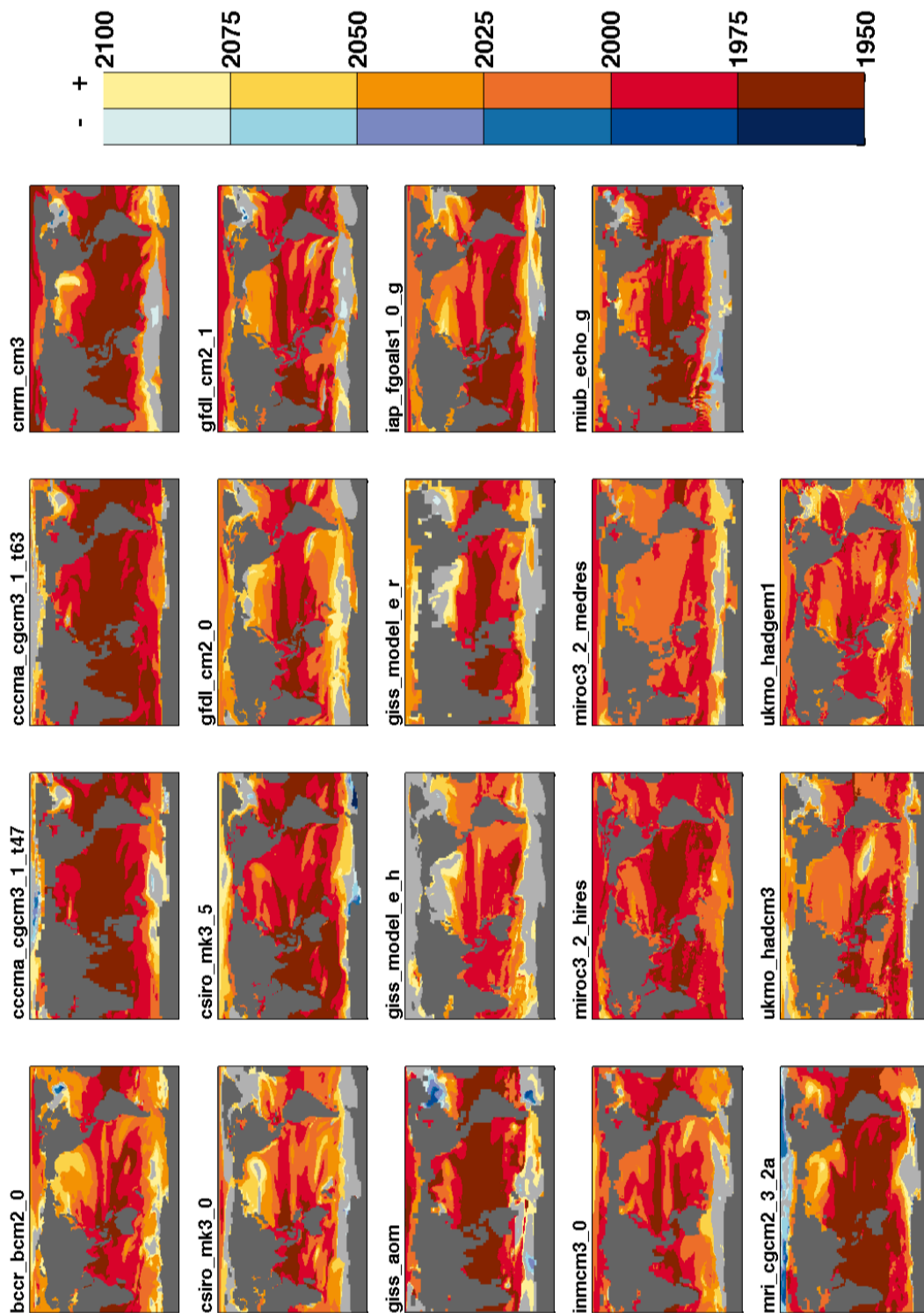


Figure 4 SST emergence times for the individual models. Blue shading represents cooling while red shading warming. Grey shading indicates no emergence by 2100.

Precipitation

Precipitation changes are arguably one of the most important effects of climate change. The observed decadal variability is calculated from the 30 year GPCP observational data set (Adler et al. 2003) (Figure 2c) and the 30-year CMAP combined

observation and reanalysis data set (Kalnay et al. 1996). The brevity of these records means that they are undoubtedly a poor estimate of the true decadal variability. The largest decadal variability is found just off the equator between 5° and 10° North and South while the equator itself has a much smaller

decadal variability. Polewards of 15°N and 15°S the variability weakens with localized peaks at 60°S and 80°N. This pattern is consistent with high mean rainfall areas having high variability and low mean rainfall areas having low variability.

The CMAP variably shows significant differences to GPCP in the Antarctic region where satellites have problems detecting rainfall (Yin et al. 2004) - little weight should be given to the observations in this region.

The models generally reproduce the pattern of observed decadal variability between 20°N and 20°S (Figure 2c). There is considerable model spread however; the ukmo_hadcm3 model has variability over twice that of the observations while the giss_aom model is half that of the observations. While the models do underestimate the observed variability in other parts of the globe they tend to simulate the broad pattern of decadal variability reasonably well. Mahlstein et al. (2012) compared observed wet season precipitation variability with model estimates and found that models broadly underestimate the observed variability.

The direction of the emergence in precipitation shows a fairly consistent pattern across the models with increases in precipitation at the equator and at mid-latitudes (Figure 3e) and reductions in precipitation or no emergence are primarily found in the subtropics of both hemispheres (Trenberth 2011).

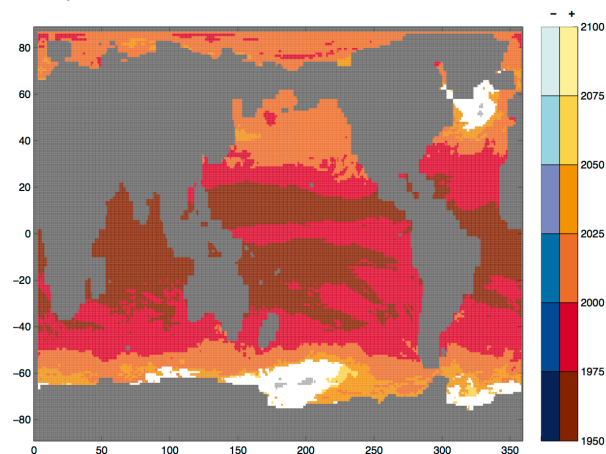


Figure 5 Sea Surface Temperature multi-model median emergence times. Colored shading is the median emergence time where 2/3 of the models agree on the sign of emergence. Red shading represents warming and blue shading a cooling. Grey shading indicates regions where 2/3 models agree on no emergence by 2100. White indicates no model agreement.

There is good model agreement to suggest that the southern hemisphere mid-latitudes are the first place to emerge with an increase in rainfall (Figure 3e). The median emergence of precipitation at 50°S

precedes both SAT or TAS. The early emergence here is due to the relatively large forced change relative to the small decadal variability (Figure 3f). Next to emerge is the region poleward of 50°N.

The equatorial region between 10°N and 10°S emerges next with an increase in precipitation and a median emergence about 50 years after the southern hemisphere mid-latitudes. While the equator has a precipitation trend that is approximately the same magnitude as the mid-latitudes, the decadal variability at the equator is approximately double that of the mid-latitudes which leads to a later emergence. The subtropics are regions of generally small mean precipitation. In both hemispheres, models show a reduction or no change in precipitation. There is high inter-model spread in emergence time, with some models showing emergence prior to the mid-latitude regions while others show no emergence by the end of the 21st century.

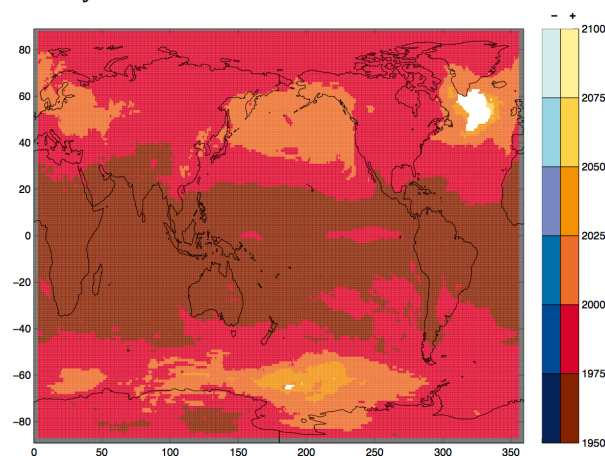


Figure 6 Atmospheric Surface Temperature multi-model median emergence times. Colored shading is the median emergence time where 2/3 of the models agree on the sign of emergence. Red shading represents warming and blue shading a cooling. Grey shading indicates regions where 2/3 models agree on no emergence by 2100. White indicates no model agreement.

While temperature exhibits relatively consistent emergence times along zonal bands, precipitation emergence is much more heterogeneous. The spatial analysis reveals a similar broad pattern on the direction of emergence with an increase in precipitation in the tropics, mid- and high-latitudes and a reduction in precipitation the subtropics (Figure 7). While there is high inter-model spread on the locations of emergence in the subtropics, all models show that some region of the subtropics emerges by 2100. The locations of these subtropical regions are predominately located over the ocean. Of the variables investigated precipitation has the largest percentage of the globe that does not emerge by 2100.

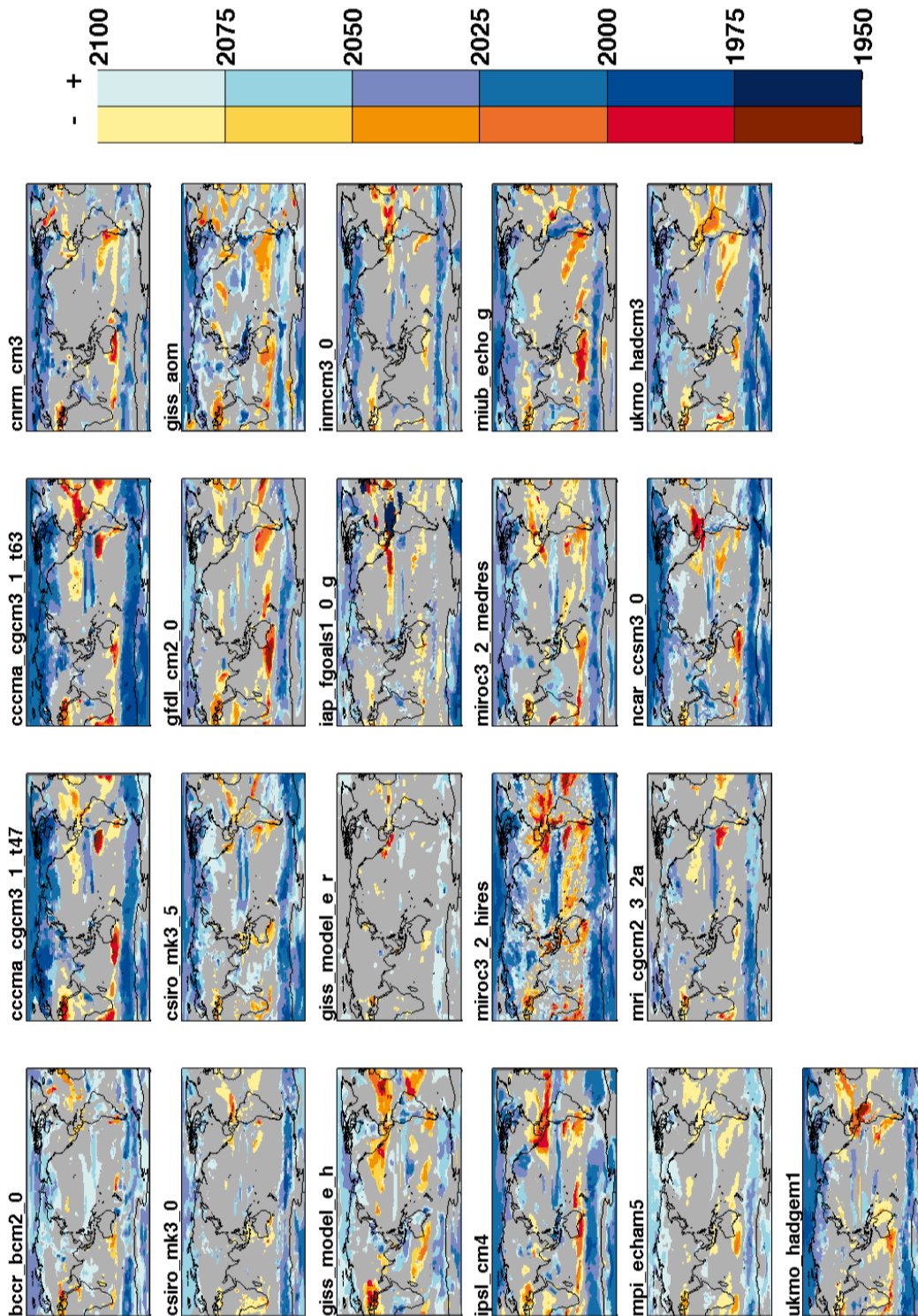


Figure 7 Precipitation emergence times for the individual models. Red shading represents decreased precipitation while blue shading increased. Grey shading indicates no emergence by 2100.

Early emergence of precipitation in the Southern Ocean is found in all of the models and is consistent with a southward shift of the storm track (Bengtsson et al. 2006). In the subtropics, the areas where there is model agreement with respect to both emergence

and the sign of the climate trends is restricted to 6 locations, South West Western Australia, South Africa, the Eastern Pacific Ocean west of Chile and Peru, the subtropical northern Atlantic Ocean, central America, and the Mediterranean (Figure 8).

Outside of the land regions poleward of 60°N and regions around the Mediterranean, agreement on emergence is restricted to regions over the oceans.

Sensitivities

The above method is sensitive to various assumptions that have been made. Some of these sensitivities are; the baseline period, the time averaging interval, the size of the emergence threshold and the assumption that precipitation is Gaussian. These assumptions are now explained and investigated here.

Increasing the time average from 10 years to 20 years in both signal and noise, results in earlier multi-model median emergence at all latitudes of between 5 and 20 years in both SST and SAT. The median time of emergence in precipitation is reduced by 20 years in the tropics and 5 years in mid-latitudes. The sub-tropical regions that did not emerge by 2100 for a 10-year average now emerge between 2060 and 2080.

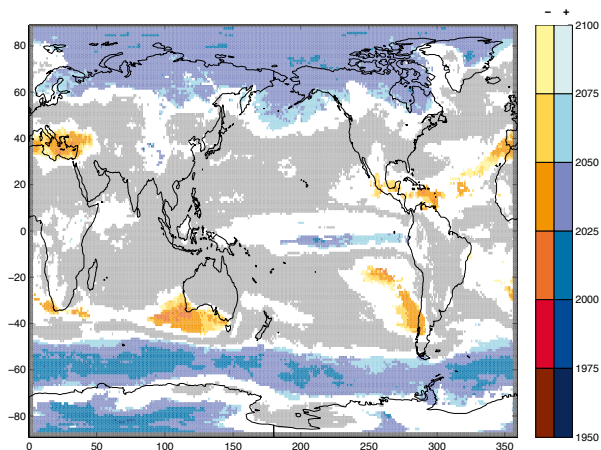


Figure 8 Precipitation, multi-model median emergence times. Colored shading is the median emergence time where 2/3 of the models agree on the sign of emergence. Grey shading indicates where 2/3 of the models agree on no emergence by 2100. Grey shading indicates regions where 2/3 models agree on no emergence by 2100. White indicates no model agreement.

Decreasing the time average from 10 years to 1-year results in the emergences of between 10 and 65 years later in both SST and TAS (Figure 9a,b). The largest differences between the 10 and 1-year averages are found within the tropics, and particularly at the equator. This is due to much more ENSO related variability within these latitudes when using 1-year averages. In precipitation, using 1-year averages results in emergence in the high latitudes 60 years later than the 10-year average, while the tropics and subtropics no longer emergence by 2100 (Figure 9c). Emergence in annual precipitation within the subtropics and tropics only occurs if the emergence threshold is reduced from three to one

standard deviation. In this case the median emergence occurs during the late 21st century.

Decreasing the emergence threshold from three standard deviations to one results in earlier emergence at all latitudes of between 10 and 35 years in all variables (Figure 9a,b,c). For precipitation the locations where there is inter-model agreement on the direction of emergence do not change. However with the reduced threshold much of the subtropics now emerge before 2100. Though there is very little agreement on the direction of change. This result is consistent with Power et al. (2012), with models disagreeing on the direction of change where the changes are small.

The method was also tested by changing the time period that changes were calculated against. When the control mean is replaced by the 1900-1930 mean, this resulted in slightly later emergence in the tropics for SST and SAT, with MMM emergence in 1970 rather than the 1950s. Outside of the tropics the MMM did not change by more than 5 years. For precipitation the MMM did not change by more than 5 years at all latitudes.

In all sensitivity tests listed above, except the annual mean, the pattern of emergence remained unchanged. The sensitivity of the results to the assumption that the time series is normally distributed was tested by comparing the emergence of one, two and three standard deviations with the equivalent distribution percentiles. The multi-model median results did not change substantively.

The results were also investigated on 5° grid using conservative interpolation and there was no substantial change in the broad spatial pattern nor times of emergence.

Discussion and Conclusions

In this study we determined the regions where the anthropogenically forced signal clearly emerges from the natural background variability both zonally and spatially at the decadal time scale. The emergence time was defined as the year when the decadal mean change relative to the pre-industrial mean (for a given property) exceeded and then remained above a natural variability threshold. This threshold was calculated based on three times the standard deviation of the pre-industrial control. Our study also investigates for the first time the emergence of decadal SST as well as decadal ocean precipitation.

The models agree that a clear anthropogenic climate change signal in both SST and near-surface atmospheric temperature will be detectable in the tropics before the high-latitudes, also found at the

decadal level in Kattsov and Sproyshev (2006) and at the seasonal level in (Mahlstein et al 2011; Hawkins and Sutton 2012). However emergence times across the models can differ by up to 150 years at high latitudes, and 100 years at low latitudes. Based on multi-model median results, SAT generally emerges before SST due to the larger signal over land compared to that over the ocean.

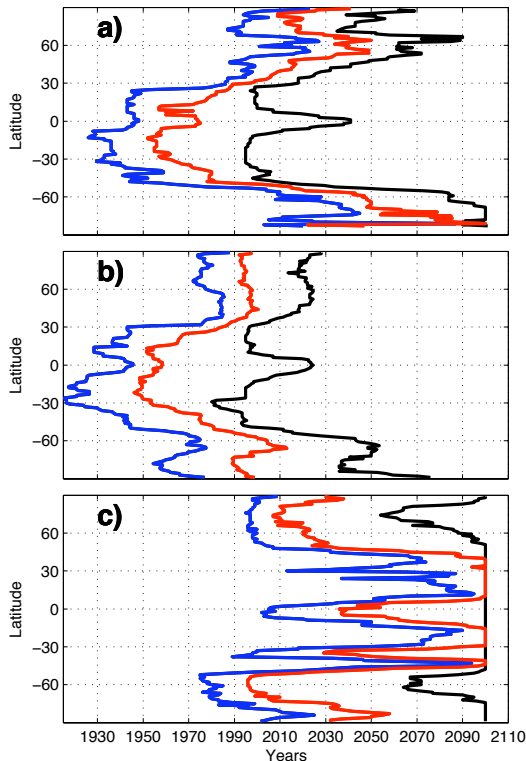


Figure 9 Multi-Model Median Time of Emergence of zonally averaged a) SST, c) SAT, e) Precipitation, for 1 year (black), 10 year mean with emergence threshold three times standard deviation of variability (red) and 10 year mean with emergence threshold one times standard deviation of variability (blue). The temporal average is calculated for both signal and noise. Median emergence at 2100 implies no emergence.

There are locations of precipitation emergence that are consistent among the models. These locations are South West Western Australia, The Mediterranean, the equatorial Pacific Ocean, the SE Atlantic Ocean, the NE Atlantic Ocean and over much of the area north of 50° N-S. The locations, and times of emergence are broadly consistent with those found by Giorgi and Bi (2009). Over much of the subtropics no emergence is detected by 2100. More in depth studies are required in these regions on the structure of precipitation and changes to it. Our method does not detect an emergence in the mean but the precipitation may have altered in different ways, this issue is important in making robust climate projections. Of the regions that do show early emergence, large changes to the precipitation have already been observed in some cases. South

West Western Australia for example has undergone a significant reduction in precipitation (Hope et al. 2006). The models suggest a median emergence time in this region before the second half of the 21st century (although earlier times are obtained using smaller emergence thresholds). The regions of emergence over land are similar to those precipitation emergence regions found in Mahlstein et al. (2012).

While the largest anthropogenic signal in air temperature occurs in the Arctic due to polar amplification, the large decadal variability there means that emergence actually occurs later than in the tropics, despite the forced signal being much smaller. This highlights the importance of being able to obtain an accurate estimate of decadal variability in determining the time of emergence. Long pre-industrial control simulations are important to resolve decadal and longer-term variability. The better the approximation of this decadal variability, the more accurate the emergence time will be. Wittenberg (2009) found that for NINO3 SST, at least 500 year periods of control data were needed in order to represent the full power spectrum (based on a 2000 year simulation). In our analysis only 8-9 models have a long pre-industrial control simulation (> 400 years, Table 1). However, when models with a pre-industrial control simulation length greater than 400 years are used (instead of our 100 year criteria) the multi-model median result does not change greatly.

This analysis only examines emergence with respect to changes in the mean state. In addition to this, changes may also occur to the magnitude and frequency of the variability, which are not considered here. In the tropical Pacific for example many of the climate models project changes to ENSO characteristics. However, in the CMIP3 models there is little consistency with regards to the direction of that change (e.g. Collins et al. 2010). Trends in the variability over time in the forced simulation could also affect the calculation of the mean state emergence time. Our use of a pre-industrial control to estimate the variability assumes that such changes are negligible.

Examination of emergence at local scales will also be affected by model biases. In the tropical Pacific a systematic bias in the spatial pattern associated with ENSO variability (Brown et al. 2012) imply that there will also be a spatial bias in the emergence time.

This study should not be used to determine the exact date that a climate signal is expected to emerge since the year of emergence is sensitive to the variability threshold used. Rather the analysis provides information on the spatial pattern of emergence

including model agreement on regions of no emergence.

Acknowledgments

We would like to thank 2 anonymous reviewers and Ben Santer for their constructive comments on a previous version. We acknowledge the modeling groups, the Program for Climate Model Diagnosis and Intercomparison (PCMDI) and the WCRP's Working Group on Coupled Modelling (WGCM) for their roles in making available the WCRP CMIP3 multi-model dataset. Support of this dataset is provided by the Office of Science, U.S. Department of Energy. We would like to also acknowledge support from the Pacific Australia Climate Change Science and Adaptation Program (PACCSAP), a program managed by the Department of Climate Change and Energy Efficiency in collaboration with AusAID, and delivered by the Bureau of Meteorology and the Commonwealth Scientific and Industrial Research Organisation (CSIRO).

References

- Adler, R., et al., 2003: The version-2 Global Precipitation Climatology Project (GPCP) monthly precipitation analysis (1979–present). *J. Hydromet.* 4 (6), 1147–1167.
- Barnett, T. P. and M. E. Schlesinger, 1987: Detecting changes in global climate induced by greenhouse gases. *J. Geophys. Res.*, 92 (D12), 14772–14780, doi:10.1029/JD092iD12p14772.
- Bengtsson, L., K. I. Hodges, and E. Roeckner, 2006: Storm tracks and climate change. *Journal of Climate*, 19 (15), 3518–3543, doi:10.1175/JCLI3815.1.
- Brown, J. N., A. Sen Gupta, et al. 2013: Implications of CMIP3 model biases and uncertainties for climate projections in the western Tropical Pacific. *Climatic Change* 119(1), 147–161, doi:10.1007/s10584-012-0603-5.
- Collins, M., et al., 2010: The impact of global warming on the tropical Pacific Ocean and El Niño. *Nature Geoscience*, 3 (6), 391–397, doi:10.1038/ngeo868.
- Diffenbaugh, N. S. and M. Scherer, 2011: Observational and model evidence of global emergence of permanent, unprecedented heat in the 20th and 21st centuries. *Clim. Change*, 107 (3–4), 615–624, doi:10.1007/s10584-011-0112-y.
- Giorgi, F. and X. Bi, 2009: Time of emergence (TOE) of GHG-forced precipitation change hot-spots. *Geophys. Res. Lett.*, 36 (6), L06 709, doi:10.1029/2009GL037593.
- Hawkins, E. and R. T. Sutton, 2012: Time of emergence of climate signals. *Geophys. Res. Lett.*, L01702, doi:10.1029/2011GL050087.
- Hope, P. K., W. Drosowsky, and N. Nicholls, 2006: Shifts in the synoptic systems influencing southwest Western Australia. *Clim. Dynam.* 26 (7–8), 751–764, doi:10.1007/s00382-006-0115-y.
- Kalnay, E., et al., 1996: The NCEP/NCAR 40-year reanalysis project. *Bull. Amer. Meteor. Soc.*, 77 (3), 437–471.
- Kanamitsu, M., W. Ebisuzaki, J. Woollen, S. Yang, J. Hnilo, M. Fiorino, and G. L. Potter, 2002: NCEP-DOE AMIP-II reanalysis (r-2). *Bull. Amer. Meteor. Soc.*, 83, 1631–1643.
- Kaplan, A., M. Cane, Y. Kushnir, A. Clement, M. Blumenthal, and B. Rajagopalan, 1998: Analyses of global sea surface temperature 1856–1991. *J. Geophys. Res.*, 103, 18567–18 589.
- Karl, T. R., R. R. Heim, and R. G. Quayle, 1991: The Greenhouse Effect in Central North America: If Not Now, When? *Science*, 251 (4997), 1058–1061, doi:10.1126/science.251.4997.1058.
- Kattsov, V. M. and P. V. Sproyshev, 2006: Timing of global warming in IPCC AR4 AOGCM simulations. *Geophys. Res. Lett.*, 33, L23 707, doi:10.1029/2006GL027476.
- Mahlstein, I., R. Knutti, S. Solomon, and P. R. W., 2011: Early onset of significant local warming in low latitude countries. *Environ. Res. Lett.*, 6, 034 009, doi:10.1088/1748-9326/6/3/034009.
- Mahlstein, I., R. W. Portmann, J. S. Daniel, S. Solomon, and R. Knutti, 2012: Perceptible changes in regional precipitation in a future climate. *Geophys. Res. Lett.*, 39, L05701, doi:10.1029/2011GL050738.
- Meehl, G. A., C. Covey, T. Delworth, M. Latif, B. McAvaney, J. F. B. Mitchell, R. J. Stouffer, and K. E. Taylor, 2007: THE WCRP CMIP3 Multimodel Dataset: A New Era in Climate Change Research. *Bull. Amer. Met. Soc.*, 88 (9), 1383, doi:10.1175/BAMS-88-9-1383.
- Power, S. B., F. Delage, R. Colman, and A. Moise, 2012: Consensus on twenty-first-century rainfall projections in climate models more widespread than previously thought. *J. Clim.*, 25, 3792–3809, doi:10.1175/JCLI-D-11-00354.1.
- Rayner, N. A., D. E. Parker, E. B. Horton, C. K. Folland, L. V. Alexander, D. P. Rowell, E. C. Kent, and A. Kaplan, 2003: Global analyses of sea surface temperature, sea ice, and night marine air temperature since the late nineteenth century. *J. Geophys. Res.*, 108 (D14), 4407, doi:10.1029/2002JD002670.
- Santer, B. D., U. Mikolajewicz, W. Brüggemann, U. Cubasch, K. Hasselmann, H. Höck, E. Maier-Reimer, and T. M. L. Wigley, 1995a: Ocean variability and its influence on the detectability of greenhouse warming signals. *J. Geophys. Res.*, 100 (C6), 10 693–10 725, doi:10.1029/95JC00683.
- Santer, B. D., K. E. Taylor, T. M. L. Wigley, J. E. Penner, P. D. Jones, and U. Cubasch, 1995b: Towards the detection and attribution of an anthropogenic effect on climate. *Clim. Dynam.*, 12 (2), 77–100, doi:10.1007/BF00223722.
- Sen Gupta, A., L. Muir, J. N. Brown, S. Phipps, P. Durack, D. Monselesan, and S. Wijffels, 2011: Climate drift in cmip3 models. *J. Clim.*, doi:10.1175/JCLI-D-11-00312.1, in press.

- Sen Gupta, A., A. Santoso, A. S. Taschetto, C. C. Ummenhofer, J. Trevena, and M. H. England, 2009: Projected changes to the southern hemisphere ocean and sea ice in the IPCC AR4 climate models. *J. Clim.*, 22, 3047–3078, doi:10.1175/2008JCLI2827.1.
- Trenberth, K. E., 2011: Changes in precipitation with climate change. *Clim. Res.*, 47, 123–138, doi:10.3354/cr00953.
- Uppala, S. M., et al., 2005: The ERA-40 re-analysis. *Q. J. R. Meteor. Soc.*, 131 (612), 2961–3012, doi:10.1256/qj.04.176.
- Wittenberg, A. T., 2009: Are historical records sufficient to constrain ENSO simulations? *Geophys. Res. Lett.*, 36 (12), L12 702, doi:10.1029/2009GL038710.
- Xie, S.-P., C. Deser, G. A. Vecchi, J. Ma, H. Teng, and A. T. Wittenberg, 2010: Global warming pattern formation: Sea surface temperature and rainfall*. *J. Clim.*, 23, 966–986, doi:10.1175/2009JCLI3329.1.
- Yin, X., A. Gruber, and P. Arkin, 2004: Comparison of the GPCP and CMAP merged gauge– satellite monthly precipitation products for the period 1979–2001. *Journal of Hydrometeorology*, 5 (6), 1207–1222, doi:10.1175/JHM-392.1.

Constraining a regional ocean model with climatology and observations: Application to the Hawaiian Islands

Peter R. Oke, Madeleine L. Cahill, David A. Griffin, Mike Herzfeld

CSIRO Marine and Atmospheric Research and

Wealth from Oceans Flagship Program, Hobart, Tasmania, Australia

peter.oke@csiro.au

Introduction

Regional ocean models are usually nested within a large-scale, often global, ocean model (hereafter called a “parent model”), to provide initial conditions and boundary forcing (e.g., De Mey et al., 2009). This means that an operational ocean forecast system that uses a regional ocean model requires reliable access to fields from a parent model. However, there are many cases when this is not possible or convenient. For example, in a situation where a regional model is to run on an isolated computer platform, such as a classified military environment, the transfer of large data sets might be problematic. In such a case, transfer of data to the classified environment might require an “air gap” – where data are copied to a disk, security-checked, and then transferred to the classified system. The transfer of large data sets may be impractical in this circumstance. This poses the question – what is the minimal data required to meaningfully constrain a regional ocean model? Could a regional ocean model be initialised and forced using an ocean climatology, plus local observations? In this study, we show that a simple Ensemble Optimal Interpolation (EnOI; Oke et al., 2002; Evensen, 2003; Oke et al., 2007, 2010) data assimilation system can constrain a regional ocean model using just atmospheric forcing, local observations and an ocean climatology. To demonstrate the efficacy of this approach, we present results for a domain centred on the Hawaiian Islands. In this paper, we describe the regional model; then the global model, from which the climatological fields and the ensemble are derived. The data assimilation system is then described, followed by results and conclusions.

Regional Model

The Relocatable Ocean Atmosphere Model (ROAM) is a key component of the Bluelink partnership between CSIRO, the Bureau of Meteorology, and the Royal Australian Navy². ROAM is a high-resolution, relocatable, semi-coupled atmosphere-ocean-wave model, which can produce a forecast out to 7 days.

Each application of ROAM is configured and run from a simple graphical user interface, allowing the user to quickly specify the model region and resolution. The ROAM system employs three physical-based models including the Sparse Hydrodynamic Ocean Code (SHOC; Herzfeld, 2009), the Regional Atmospheric Modelling System (RAMS; Cotton et al., 2003), and the Simulating WAVes Nearshore (SWAN) model (Booij et al., 1999). The focus of this study is on the performance of SHOC, the ocean component of ROAM. SHOC solves the primitive equations on z-levels using a computationally efficient sparse coordinate system (Herzfeld, 2009). For the configurations presented here, SHOC uses the level-2 turbulence sub-model of Mellor and Yamada (1982), and an advection scheme called QUICKEST (Leonard, 1991).

For the case study presented in this study, the model is configured with horizontal grid spacings of ~5 km. There are 43 vertical levels, with 4 m resolution near the surface and 16 layers over the top 190 m depth. The topography for SHOC is derived from the 30 arc-second GEBCO_08 topography for most of the world, and a 9 arc-second topography produced by Geoscience Australia (Whiteway, 2009). Horizontal diffusion is zero away from the horizontal boundaries, and increases over a sponge layer within 5 grid points of each boundary. The horizontal viscosity is resolution and state-dependent according to the Smagorinsky viscosity scheme (Griffies and Hallberg, 2000).

For most cases, SHOC temperature and salinity is initialised with fields from either the Bluelink ReANalysis (BRAN; Oke et al., 2013b) or the operational Bluelink forecast system, called OceanMAPS (Brassington et al., 2007) – both of which are produced using the Ocean Forecast Australia Model (OFAM; Oke et al., 2013a) and the Bluelink Ocean Data Assimilation System (BODAS; Oke et al., 2008, 2013b). When integrated in semi-coupled mode, SHOC is forced at the surface with fluxes derived from RAMS. However, for the example presented here, we use 3-hourly fluxes of heat and

² <http://wp.csiro.au/bluelink/>

momentum derived from the ERA-Interim atmospheric reanalysis (Dee and Uppala, 2009). The horizontal boundary conditions for SHOC include an upstream advection condition for temperature and salinity – so when the flow is directed into the domain the boundary values are used, and when the flow is directed out of the domain the interior values are used. The boundary values for sea-level and velocity are set so that the net volume transport through all open boundaries is forced to zero after every barotropic time-step.

Global Model

The Bluelink ocean model, called OFAM, has been developed over many years. The latest version of OFAM (OFAM3; Oke et al., 2013a) is used in this study to construct the climatological fields, which are the background fields for the data assimilation. OFAM3 fields are also used to construct the ensemble, which underpins the data assimilation system. Details are presented in section 4, below.

OFAM3 is eddy-resolving ($1/10^\circ$ grid spacings) for all longitudes and between 75°S - 75°N , and is a configuration of the GFDL Modular Ocean Model (Griffies et al., 2004, MOM4p1). OFAM3 has 5 m vertical grid spacings at the ocean surface that increases gradually to 10 m vertical grid spacings over the top 200 m, and coarser below that (with a total of 51 vertical levels). OFAM3 is forced with 1.5° -resolution, 3-hourly surface heat, freshwater, and momentum fluxes from ERA-interim (Dee and Uppala, 2009). Like SHOC, the topography for OFAM3 is derived from GEBCO 08 topography (www.bodc.ac.uk/data/online_delivery/gebco/) and Geoscience Australia (Whiteway, 2009). Vertical mixing is parameterised by the hybrid mixed-layer scheme of Chen et al. (1994), plus implicit tidal mixing using the scheme described by Lee et al. (2006). Horizontal mixing is based on the Smagorinsky scheme (Griffies and Hallberg, 2000).

OFAM has been used for many studies, including ocean reanalyses (Oke et al., 2005, 2008; Schiller et al., 2008; Oke et al., 2013b), observing system experiments (Oke and Schiller, 2007), an investigation of a series of coral bleaching events in the Great Barrier Reef (Schiller et al., 2009), an analysis of eddy dynamics in the Tasman Sea (Oke and Griffin, 2011), an analysis of fronts in the Southern Ocean (Langlais et al., 2010), an investigation of the seasonality of Chlorophyll a in anti-cyclonic eddies off Western Australia (Dietze et al., 2009), and climate downscaling (Sun et al., 2012). An operational version of OFAM2 is run at the Bureau of Meteorology and is described by Brassington et al. (2007).

Data Assimilation

The latest version of BODAS (version 8.3) that is used here is described by Oke et al. (2013b). BODAS is an EnOI-system (Oke et al., 2002; Evensen, 2003). EnOI is based on the Ensemble Kalman Filter (EnKF; Evensen, 1997, 2003), but it uses a time-invariant ensemble to approximate the system's background error covariance. EnOI is inexpensive and robust, and has been tested and shown to be effective for a range of ocean applications (e.g., Oke et al., 2005, 2007, 2008, 2009, 2010, 2013b; Counillon et al., 2009; Fu et al., 2009; Counillon and Bertino, 2009; Wan et al., 2010; Xie and Zhu, 2010; Srinivasan et al., 2011). EnOI uses a time-invariant ensemble that is derived from OFAM3. We use 144 ensemble members. Each member is constructed by subtracting a 3-day mean field from a 3-month mean field for the centre of each month, for the last 12 years of the OFAM3 run described by Oke et al. (2013a).

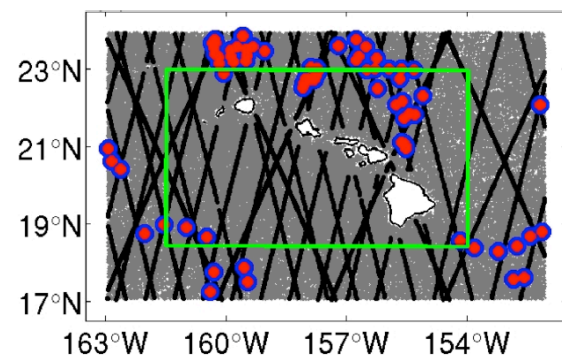


Figure 1 Map showing the extent of the model domain (green) and the location of assimilated observations of SST (grey), SLA (black), temperature (blue) and salinity (red) profiles. The locations of all assimilated observations used in the 60-day period are shown. The coverage of the SST observations denotes the domain for which analyses are computed during the assimilation step.

The implementation used here employs a local analysis (Sakov and Bertino, 2011), with the impact of each observation restricted to within 250 km of the observation location.

Both in situ and satellite observations are assimilated in a single step by BODAS. For the case presented here, we run a 60-day integration starting on 1 January 2008. Sea-level anomaly (SLA) data from ERS-2, Jason-1, and Envisat are assimilated (accessed from RADS in August 2012). Satellite sea-surface temperature data are sourced from AMSR-E (~ 25 km resolution) and NAVO (AVHRR; ~ 4 km resolution), using the preprocessing steps described by Andreu-Burillo et al. (2010). In situ profiles of temperature and salinity are assimilated from Argo. The distribution of assimilated observations for the

60-day integration period is shown in Figure 1.

Before each assimilation step, all observations that are available for assimilation are pre-processed. Along-track SLA and SST observations are combined to form super-observations so that there is no greater than one “super-observation” for every $0.1 \times 0.1^\circ$ box (the resolution of the ensemble). Similarly, the in situ profiles that are available for assimilation are “thinned” prior to assimilation, so that no greater than one profile of each type (i.e., temperature and salinity) is assimilated for every $0.1 \times 0.1^\circ$ box. Super-obing of SLA and SST, and sub-sampling of profiles is not essential here – but there is little point in retaining observations on the sub-grid-scale of the ensemble. They either represent sub-grid-scale features that cannot be represented by the ensemble, or represent redundant information.

For the case presented here, we calculate an analysis for every day of the model run. The analyses use only the OFAM3 climatological fields (a fixed database), and the ensemble (also, a fixed database). The background field (including temperature, salinity, velocity, and sea-level) for each day is from the OFAM3 climatology that is derived from the last 18-years of a 33-year model run Oke et al. (2013a), yielding a seasonally varying climatology. For this study, the background field for each assimilation step is the OFAM3 climatology for the year-day of each analysis.

An analysis for every day of the model integration period is computed before the regional model integration begins, and analyses are concatenated yielding a time-series of the three-dimensional ocean circulation (including all variables) for a region that is slightly larger than the regional model domain (marked by the region spanned by observations in Figure 1). All analyses are computed on a sub-set (cookie-cut out) of the OFAM3 grid (with a $1/10^\circ$ horizontal grid). These analysis fields are used to initialise, constrain, and force the regional model. The initial conditions are constructed by simply interpolating the temperature, salinity, velocity, and sea-level fields from the analysis at the start of the model run, onto the regional model’s grid. The analysis fields are used during the model integration to provide a weak constraint on the temperature and salinity, by nudging towards the four-dimensional analyses continuously using a restoring time-scale of 3 days. Analysis fields are also incorporated into the open boundary conditions throughout the model run. The role of the regional model is to dynamically “filter” the three-dimensional analysis fields. As SHOC is nudged towards the analyses – and set to analysis values at the boundaries, the regional model

eliminates dynamically inconsistent features and generates other dynamical features that are not present in the analyses.

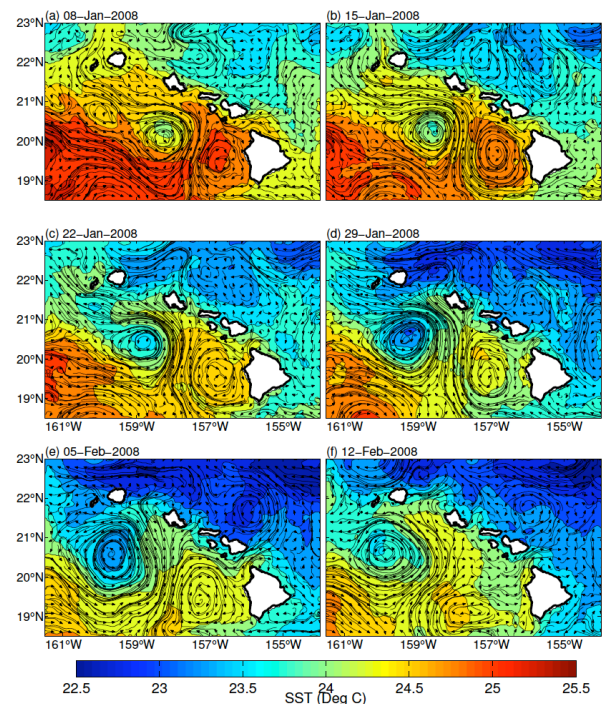


Figure 2 A weekly series of daily mean SST and near-surface velocity (15 m depth) for the domain around Hawaii.

Results

We assess the outlined approach for an open-ocean case around the Hawaiian Islands – a challenging application, with four open boundaries and circulation that is largely remotely driven. The domain used here is shown in Figure 1.

A series of examples of the model fields are shown in Figure 2 to demonstrate the complexity of the circulation. This sequence of fields demonstrates that during the experiment period the circulation is quite complicated, with several mesoscale eddies developing and moving through the domain. There is a distinct difference in the water temperature from the colder waters to the north and east of the Hawaiian Islands, to the warmer waters to the south. An energetic cyclonic eddy forms near the centre of the model domain near the start of the model run, then slowly advects to the west. The temperature in the centre of the cyclonic eddy is several degrees colder than the surrounding waters. The sequence of model fields shown in Figure 2 demonstrates that the circulation is not trivial. It includes instabilities, and evolution on short spatial scales (inc. the sub-mesoscale) and on short time-scales.

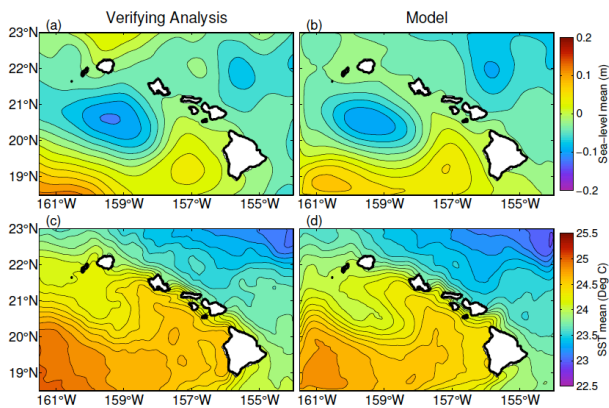


Figure 3 Comparison of the mean (a-b) sea-level and (c-d) SST from (a,c) the verifying analysis and (b,d) the model for the case study being presented.

The time-mean sea-level and SST are shown in Figure 3. Included in Figure 3 are fields from the model - and fields from the verifying analysis. Recall that for each day of the model run, local observations (Figure 1) are combined with climatological fields to construct an analysis. These daily analyses are here referred to as verifying analyses. Note that they are therefore not independent of the model run. However, note that this study is intended to be a first step towards the development of a regional ocean forecasting capability – so we must first determine whether a high-resolution regional model can be initialised and constrained using the proposed approach. In a subsequent study, we will explore the usefulness of this approach for initialising a forecast.

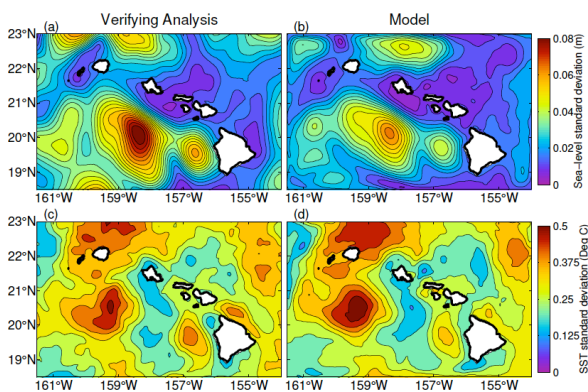


Figure 4 Comparison of the standard deviation of (a-b) sea-level and (c-d) SST from (a,c) the verifying analysis and (b,d) the model for the case study being presented.

For each verifying analysis, the fields of SLA and SST agree with observations to within about 0.06 m and 0.25°C, respectively. The verifying analyses are used to initialise the model – and to constrain the regional model at the boundary, and at the interior (with a weak 3-day restoring). Figure 3 shows that the mean circulation generated by the regional model is in close agreement with the verifying analysis. The

<http://www.cawcr.gov.au/publications/researchletters.php>

footprint of the cyclonic eddy, referred to above, is evident in the mean field – identified by the negative SLA of about 10 cm, centred at around 159°W.

To assess the variability of the modelled fields, we compare the standard deviation of sea-level and SST in Figure 4, using daily mean model fields and daily analyses. Some differences between the model fields and the verifying analyses are evident. However, in general, there is good agreement between the analysed and modelled variability. This indicates that the approach used in this study is effective at constraining the sub-mesoscale circulation generated by the regional model.

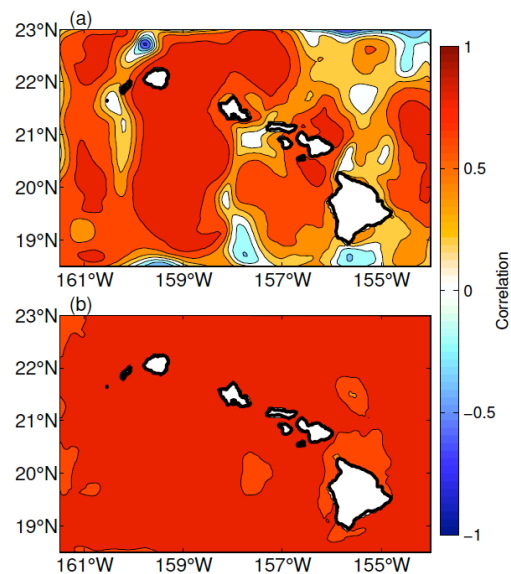


Figure 5 Correlation between the modelled and analysed (a) sea-level and (b) SST for the Hawaii case study.

Maps of the correlation between the modelled and analysed sea-level and SST are shown in Figure 5. These maps show that the modelled variability is very well aligned with the analysed fields – with almost perfect correlation between the modelled and analysed SST; and high correlations in most of the domain for SLA. Correlations between the modelled and analysed SLA are lower in some regions, particularly along the northern boundary, where the modelled circulation is mostly flowing out of the domain (see Figure 2).

A comparison between the modelled sub-surface temperature and the observed temperature from unassimilated data is presented in Figure 6. Expendable-BathyThermograph (XBT) observations presented here were not assimilated. Included in Figure 6 are the observed and modelled fields; plus the differences between the observed temperature and the temperature from the regional model, and from the analyses.

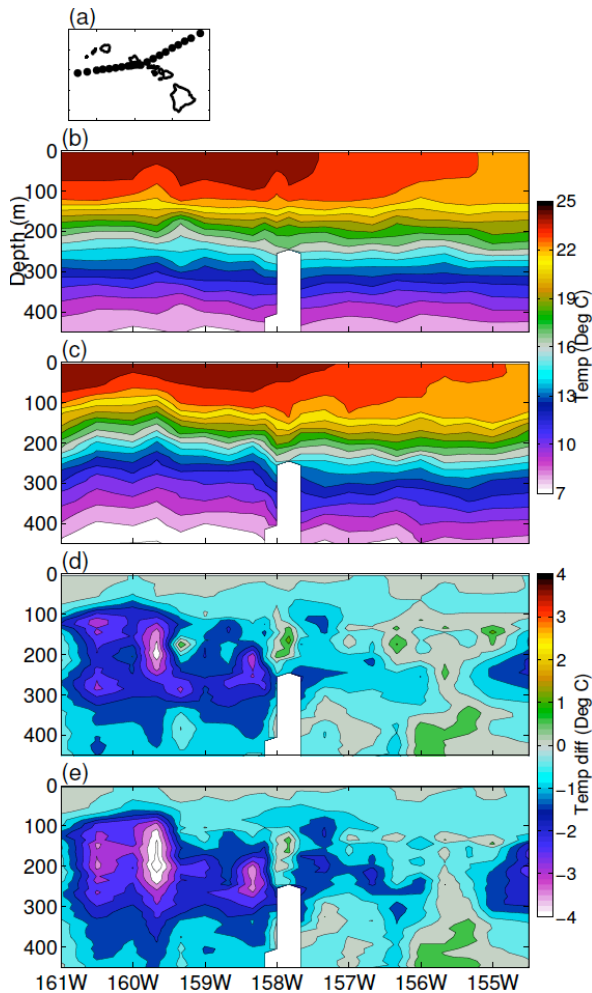


Figure 6 Temperature section along (a) an XBT transect (PX-34) showing the (b) observed and (c) modelled temperature over the top 450 m; and the difference between the observed temperature and the (d) modelled and (e) analysed temperature. The XBT section spanned 16-18 February 2008.

In general, there is good agreement between the modelled and independently-observed sub-surface temperature. The largest difference is evident west of 160°W. This difference is due to the lack of assimilated sub-surface observations in that region (see Figure 1). There were only a handful of Argo profiles to the south-west of the model domain that apparently provided a weaker constraint on the analyses. This highlights a limitation of the approach used here – namely that in observation-sparse regions, the constructed analyses may have significant errors. Interestingly, the difference between the XBT temperature and the regional model temperature is smaller than the XBT temperature and the analyses. This indicates that in this case, the model adds some value – improving on the analyses, by including the impacts of local forcing and local dynamics.

Conclusions

In this study, we're motivated to determine whether it is feasible to constrain a high-resolution regional ocean model using only climatology and local observations. Such an undertaking eliminates the dependency of nesting the regional ocean model in a large-scale parent model. This might be important for situations where access to fields from a parent model are either unreliable, or bandwidth limited. Such a situation may occur when a regional model is to be run on a classified system, where the system is isolated from the Internet.

We've shown that for an open-ocean case we can use a simple, efficient data assimilation approach, based on EnOI, to initialise and constrain the sub-mesoscale variability of a regional ocean model. The generated model fields are complex, including eddies, and complex circulation patterns. However, we've shown that the modelled mean state, and the modelled variability is in close alignment with assimilated observations; and is in good agreement with independent, with-held observations. Although this is only a first step towards the development of an operational, regional ocean forecasting capability, this case study demonstrates that it is feasible. Additional case studies will be considered in future to assess the robustness of our results. Another important step is the verification that a model that is initialised using the approach described here can yield a skillful forecast. If found to be robust, the approach described here could be used routinely either alongside more conventional approaches, or independently.

Acknowledgments

Financial support for this research is provided by CSIRO, the Bureau of Meteorology and the Royal Australian Navy as part of the Bluelink project, and the US Office of Naval Research. The authors also acknowledge the contributions of the Bluelink Science Team. Satellite altimetry is provided by NASA, NOAA and CNES. SST observations are provided by NOAA and Remote Sensing Systems.

References

- Andreu-Burillo, I., Brassington, G. B., Oke, P. R., Beggs, H., 2010. Including a new data stream in the Bluelink ocean data assimilation system. *Aust Meteorol Ocean* 59, 77-86.
- Booij, N., Ris, R. C., Holthuijsen, L. H., 1999. A third-generation wave model for coastal regions: 1. model description and validation. *Journal of Geophysical Research: Oceans* 104 (C4), 7649-7666. URL <http://dx.doi.org/10.1029/98JC02622>.
- Brassington, G. B., Pugh, T. F., Spillman, C., Schulz, E., Beggs, H., Schiller, A., Oke, P. R., 2007. Bluelink development of operational oceanography and servicing in Australia. *J*

- Research Pract Inf Tech 39 (2), 151-164.
- Chen, D., Rothstein, L., Busalacchi, A., 1994. A hybrid vertical mixing scheme and its application to tropical ocean models. *Journal of Physical Oceanography* 24 (10), 2156-2179.
- Cotton, W. R., Pielke Sr., R. A., Walko, R. L., Liston, G. E., Tremback, C. J., Jiang, H., McAnelly, R. L., Harrington, J. Y., Nicholls, M. E., Carrio, G. G., McFadden, J. P., 2003. Rams 2001: Current status and future directions. *Meteorology and Atmospheric Physics* 82 (1-4), 5-29. URL <http://dx.doi.org/10.1007/s00703-001-0584-9>
- Counillon, F., Bertino, L., 2009. Ensemble optimal interpolation: multivariate properties in the Gulf of Mexico. *Tellus A* 61 (2), 296-308.
- Counillon, F., Sakov, P., Bertino, L., 2009. Application of a hybrid EnKF-OI to ocean forecasting. *Ocean Science* 5 (4), 389-401.
- De Mey, P., Craig, P., Davidson, F., Edwards, C. A., Ishikawa, Y., Kindle, J. C., Proctor, R., Thompson, K. R., Zhu, J., 2009. Applications in coastal modelling and forecasting. *Oceanography* 22, 198-205.
- Dee, D. P., Uppala, S., 2009. Variational bias correction of satellite radiance data in the ERA-interim reanalysis. *Quarterly Journal of the Royal Meteorological Society* 135 (644), 1830-1841.
- Dietze, H., Matear, R., Moore, T., 2009. Nutrient supply to anticyclonic meso-scale eddies off Western Australia estimated with artificial tracers released in a circulation model. *Deep Sea Research* 56, 1440-1448.
- Evensen, G., 1997. Advanced data assimilation for strongly nonlinear dynamics. *Monthly Weather Review* 125 (6), 1342-1354.
- Evensen, G., 2003. The ensemble Kalman Filter: Theoretical formulation and practical implementation. *Ocean Dynamics* 53 (4), 343-367.
- Fu, W., Zhu, J., Yan, C., 2009. A comparison between 3DVAR and EnOI techniques for satellite altimetry data assimilation. *Ocean Modelling* 26 (3-4), 206-216.
- Griffies, S. M., Hallberg, R. W., 2000. Biharmonic friction with a Smagorinsky-like viscosity for use in large-scale eddy-permitting ocean models. *Monthly Weather Review* 128 (8), 2935-2946.
- Griffies, S. M., Pacanowski, R. C., Rosati, A., 2004. A technical guide to MOM4. GFDL ocean group technical report no. 5. NOAA/Geophysical Fluid Dynamics Laboratory 5.
- Herzfeld, M., 2009. Improving stability of regional numerical ocean models. *Ocean Dynamics* 59 (1), 21-46.
- Langlais, C., Schiller, A., Oke, P. R., 2010. Southern ocean fronts in the Bluelink reanalysis. *Mercator Quarterly Newsletter* 36, 50-57.
- Lee, H.-C., Rosati, A., Spelman, M., 2006. Barotropic tidal mixing effects in a coupled climate model: ocean conditions in the northern Atlantic. *Ocean Modelling* 11, 464-470.
- Leonard, B. P., 1991. The ULTIMATE conservative difference scheme applied to unsteady one-dimensional advection. *Computational Methods in Applied Mechanical and Engineering* 19, 17-74.
- Mellor, G. L., Yamada, T., 1982. Development of a turbulence closure model for geophysical fluid problems. *Reviews of Geophysics* 20 (4), 851-875, dx.doi.org/10.1029/RG020i004p00851/
- Oke, P. R., Allen, J. S., Miller, R. N., Egbert, G. D., Kosro, P. M., 2002. Assimilation of surface velocity data into a primitive equation coastal ocean model. *Journal of Geophysical Research* 107 (C9), 3122.
- Oke, P. R., Brassington, G. B., Griffin, D. A., Schiller, A., 2008. The Bluelink Ocean Data Assimilation System (BODAS). *Ocean Modelling* 21 (1-2), 46-70.
- Oke, P. R., Brassington, G. B., Griffin, D. A., Schiller, A., 2010. Ocean data assimilation: a case for ensemble optimal interpolation. *Aust Meteorol Ocean* 59, 67-76.
- Oke, P. R., Griffin, D. A., 2011. The cold-core eddy and strong upwelling off the coast of New South Wales in early 2007. *Deep Sea Research* 58 (5), 574-591.
- Oke, P. R., Griffin, D. A., Schiller, A., Matear, R. J., Fiedler, R., Mansbridge, J. V., Lenton, A., Cahill, M., Chamberlain, M. A., Ridgway, K., 2013a. Evaluation of a near-global eddy-resolving ocean model. *Geoscientific model development* 6, 591-615.
- Oke, P. R., Sakov, P., Cahill, M. L., Dunn, J. R., Fiedler, R., Griffin, D. A., Mansbridge, J. V., Ridgway, K. R., Schiller, A., 2013b. Towards a dynamically balanced eddy-resolving ocean reanalysis: BRAN3. *Ocean Modelling* 67, 52-70.
- Oke, P. R., Sakov, P., Corney, S. P., 2007. Impacts of localisation in the EnKF and EnOI experiments with a small model. *Ocean Dynamics* 57 (1), 32-45.
- Oke, P. R., Sakov, P., Schulz, E., 2009. A comparison of shelf observation platforms for assimilation in an eddy-resolving ocean model. *Dynamics of Atmospheres and Oceans* 48 (1-3), 121-142.
- Oke, P. R., Schiller, A., 2007. Impact of Argo, SST, and altimeter data on an eddy-resolving ocean reanalysis. *Geophysical Research Letters* 34 (19), L19601.
- Oke, P. R., Schiller, A., Griffin, D. A., Brassington, G. B., 2005. Ensemble data assimilation for an eddy-resolving ocean model of the Australian region. *Quarterly Journal of the Royal Meteorological Society* 131 (613), 3301-3311.
- Sakov, P., Bertino, L., 2011. Relation between two common localisation methods for the EnKF. *Computational Geoscience* 15, 225-237.
- Schiller, A., Oke, P. R., Brassington, G. B., Entel, M., Fiedler,

- R., Griffin, D. A., Mansbridge, J. V., 2008. Eddy-resolving ocean circulation in the Asian-Australian region inferred from an ocean reanalysis effort. *Progress in Oceanography* 76 (3), 334-365.
- Schiller, A., Ridgway, K. R., Steinberg, C. R., Oke, P. R., 2009. Dynamics of three anomalous SST events in the Coral Sea. *Geophysical Research Letters* 36, L06606.
- Srinivasan, A., Chassignet, E. P., Bertino, L., Brankart, J. M., Brasseur, P., Chin, T. M., Counillon, F., Cummings, J. A., Mariano, A. J., Smedstad, O. M., Thacker, W. C., 2011. A comparison of sequential assimilation schemes for ocean prediction with the HYbrid Coordinate Ocean Model (HYCOM): Twin experiments with static forecast error covariances. *Ocean Modelling* 37, 85-111.
- Sun, C., Feng, M., Matear, R., Chamberlain, M., Craig, P., Ridgway, K., Schiller, A., 2012. Marine downscaling of a future climate scenario for Australian boundary currents. *Journal of Climate* 25, 2947-2962.
- Wan, L., Bertino, L., Zhu, J., 2010. Assimilating altimetry data into a HYCOM model of the Pacific: Ensemble optimal interpolation versus ensemble Kalman filter. *Journal of Atmospheric and Oceanic Technology* 27 (4), 753-765.
- Whiteway, T. G., 2009. Australian bathymetry and topography grid. *Geoscience Australia Record* 21, pp46.
- Xie, J., Zhu, J., 2010. Ensemble optimal interpolation schemes for assimilating Argo profiles into a hybrid coordinate ocean model. *Ocean Modelling* 33 (3-4), 283-298.

Impact of Satellite Observations on Southern Hemisphere Forecasts from the Operational ACCESS-G NWP Model

J. Lee, J. Le Marshall, C. Tingwell, B. Roux

The Centre for Australian Weather and Climate Research

Bureau of Meteorology, Melbourne, Australia

j.lee@bom.gov.au

Introduction

Satellite observations are a vital source of data for high quality forecasts from Numerical Weather Prediction (NWP) models and their beneficial impact has been demonstrated quantitatively in a number of studies (Zapotocny et al. 2007; Bouttier and Kelly 2001; Kelly and Thepaut 2007). Thanks to the coverage and quality of satellite data, and the sophistication of the current assimilation methods which are able to make better use of those observations, satellite data are the single biggest contributor to NWP forecast quality. This is more the case in the Southern Hemisphere where because of the sparsity of the conventional observational network satellite observations are crucial in defining the initial state of the atmosphere in NWP models.

Various configurations of the Australian Community Climate and Earth Simulator (ACCESS) model have recently become operational (Puri et al. 2010). ACCESS is based on the UK Met Office's Unified Model (UM). Its dynamical core uses semi-implicit and semi-Lagrangian formulation (Davies et al. 2005); various physical parametrisation schemes are employed to approximately represent some of the unresolved physical processes (Milton and Earnshaw 2007). The data assimilation component is the 4-dimensional variational data assimilation scheme (4DVAR, see Rawlins et al. 2006). ACCESS-G is a global version of UM and 4DVAR and has recently undergone an upgrade (Fraser, 2012).

One of the well-established methods of assessing the impact of observations in an NWP model is the data denial or Observing System Experiment (OSE) where one set of observations are removed from the assimilation and the resulting forecast quality is assessed (see Bouttier and Kelly 2001). Using this methodology this paper assesses the importance of satellite observations in the current operational ACCESS-G model. A standard verification score is used to assess forecast quality. The assessment will focus on the Southern Hemisphere as the role of satellite observations for the medium range forecasts for the Australian continent is of great

importance for the forecast and warning services the Australian Bureau of Meteorology provides to the Australian community. Finally this paper presents a case study that highlights the importance of satellite observations for quantitative rainfall prediction in a specific synoptic situation.

Satellite Data Usage by ACCESS-G

ACCESS-G processes all observational data using the Observation Processing System (OPS). During each analysis cycle OPS carries out a number of tasks including observation quality control, bias correction, and data thinning. Quality-controlled observations are then passed to 4DVAR data assimilation where these observations are merged with a first guess from a short-term model forecast to produce an analysis. The resulting analysis is the minimum variance estimate that combines the 4-dimensionally distributed observations and the first guess taking into account the statistical error characteristics of observations and the model background. This analysis is the initial condition from which the NWP model integration starts.

ACCESS-G assimilates varied types of observations. A well-established conventional observation network consists of SYNOP (both from ship and land-based), drifting buoys and radiosondes and these observations still form an important component of the global observing system for the atmospheric data analysis despite the huge increase in remotely sensed data. Temperature and wind reports from aircraft (AMDARs and AIREPs) are becoming increasingly important part of this conventional observation network. Data from wind profilers in the form of wind retrievals are the newest addition to the conventional network.

Despite the coverage provided by conventional observations by far the largest number of observations – more particularly for the southern hemisphere – comes from instruments from various satellite platforms. One of the most successful series of such meteorological satellite programs is the NOAA series of polar-orbiting satellites. The

principal instrument onboard is the Advanced TIROS Operational Vertical Sounder (ATOVS) which is a package of instruments comprising an infrared sounder (High-resolution Infra-Red Sounder or HIRS) and two microwave sounders (Advanced Microwave Sounder Unit A and B or AMSU-A and AMSU-B).

Hyperspectral spectrometers are instruments that collect radiation at much narrower spectral intervals and hence their spectral resolution is much higher than their predecessors like HIRS. This allows a potential increase in the vertical resolution achievable by a retrieval or during a direct radiance assimilation compared to using ATOVS. Currently there are two operational hyperspectral infrared sounders - AIRS and IASI - flown on two different platforms: one on NASA's EOS-2 satellite and the other on European Space Agency's (ESA) MetOp satellite respectively.

Besides the radiance measurements, which are directly assimilated in 4DVAR for the analysis of the temperature and humidity field there are other satellite-born remotely sensed sources of data.

Scatterometers measure microwave backscatter signals off ocean waves and give an estimate of boundary layer wind speed and direction. Currently ACCESS-G assimilates only one scatterometer, namely ASCAT. GPS-RO (Global Position System Radio Occultation) is an important source of high quality, near-bias-free observations which helps to "anchor" the analysis (Le Marshall et al. 2012). The observations are sensitive to refractivity gradients which in turn are related to temperature gradients in the stratosphere and to moisture gradients in the lower troposphere. Atmospheric motion vectors (AMVs) derived from geostationary visible and IR measurements are an important source of wind information for the analysis. Table 1 lists various observation types and their usage statistics in 4DVAR data assimilation of APS1 ACCESS-G. Figures 1 to 5 show geographic coverage of selected data types used by 4DVAR in a typical analysis cycle. For this example the base time of the analysis is 20130610 00 UTC and the coverage plots show observations falling within the 4DVAR assimilation window - 20130609 21 UTC (T-3) and 20130610 03 UTC (T+3).

Table 1 Observation types and typical observation counts used by the operational APS1 ACCESS-G 4DVAR analysis. The base date/time of the analysis is 20130610 00 UTC. The observed parameters are surface pressure (p^*), temperatures (T), relative humidity (RH), winds (u/v), brightness temperature (T_B), bending angle (α), 10-m winds (u_{10}/v_{10}). Note that for satellite radiances the observation count indicates potential number of field-of-views (FOVs) passed to 4DVAR and each FOV contains radiance measurements in multiple channels.

Observation type	Platform	Observed parameters	Primary model variables constrained by observation ^A	Obs count (number) ^B	Obs count (%) ^C
SYNOP	land, ship	P^* , T , RH , u_{10}/v_{10}	p , T , q , u/v	21667	12.3
BUOY	ocean	P^* , T , RH , u_{10}/v_{10}	p , T , q , u/v	5065	2.9
Sonde/TEMP	land, ship	T , RH , u/v	T , q , u/v	646	0.4
Sonde/PILOT	land, ship	u/v	u/v	103	0.1
Wind profiler	land	u/v	u/v	405	0.2
AMDAR	aircraft	T , u/v	T , u/v	19967	11.3
AIREP	aircraft	T , u/v	T , u/v	2411	1.4
ATOVS/HIRS	NOAA, MetOp	T_B	T	30622	17.4
ATOVS/AMSU-A	NOAA, MetOp	T_B	T	30622	17.4
ATOVS/AMSU-B	NOAA, MetOp	T_B	q	30622	17.4
AIRS	Aqua (EOS2)	T_B	T , q	5232	3.0
IASI	MetOp	T_B	T , q	7978	4.5
AMV	MTSAT, GOES, Meteosat	u/v	u/v	12890	7.3
GPSRO	GRAS/MetOp, CHAMP/COSMIC	α	T , q	477	0.3
ASCAT	MetOp	u_{10}/v_{10}	u_{10}/v_{10}	7393	4.2

^AThe multivariate nature of 4DVAR analysis means that all model fields are modified. However, what is shown are model variables directly influenced by the observations. ^{B,C}The observation counts and percentages can vary from one analysis cycle to next. ^CRounding means that the percentages for all observation types may not add up to 100%.

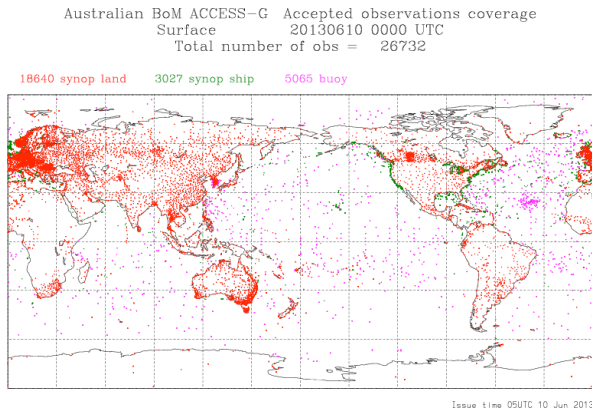


Figure 1 Observation coverage for the surface observations (SYNOP stations, drifting and moored buoys) for the analysis base time of 20130610 00 UTC.

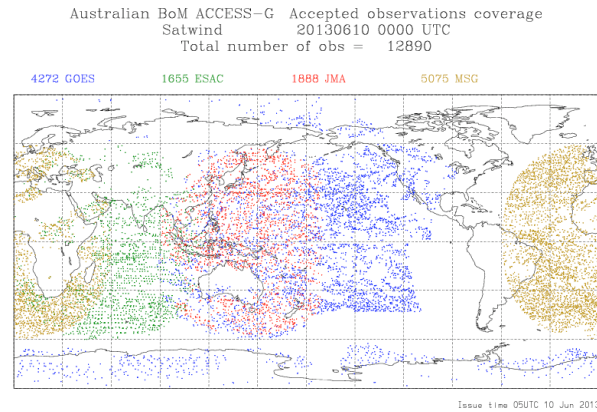


Figure 4 Observation coverage for atmospheric motion vectors (AMVs) derived from tracking cloud features using JMA, GOES and Meteosat geostationary satellite data.

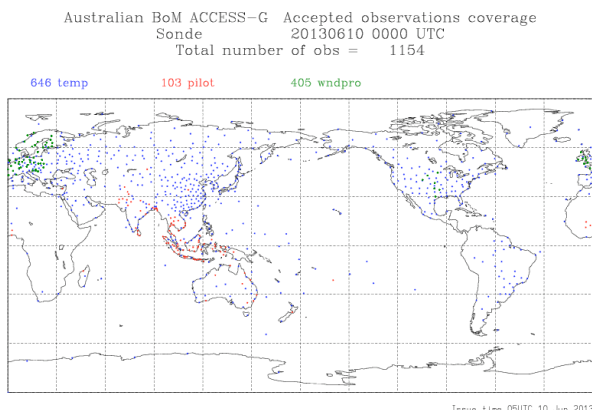


Figure 2 Observation coverage for the upper-air radiosonde and wind profiler data. The coverage is for the same analysis base time as that shown in Fig 1.

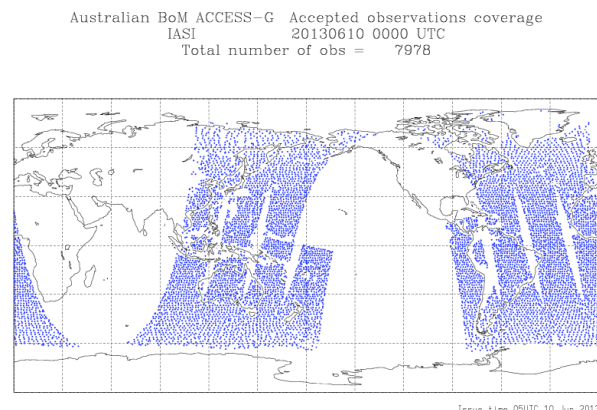


Figure 5 Observation coverage for the IASI hyperspectral instrument onboard MetOp. Each dot represents a single FOV which consists of multiple IR channels.

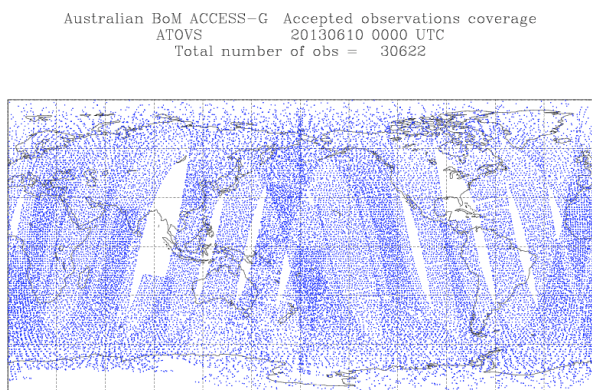


Figure 3 Observation coverage for ATOVS (HIRS, AMSU-A and AMSU-B) from MetOp and NOAA-series polar-orbiting satellites. Each dot represents a single field-of-view (FOV), which consists of multiple IR and MW channels.

Assimilation of Satellite Radiances

All infrared (IR) and microwave (MW) sounding radiometers measure upwelling radiation in different parts of electromagnetic spectrum in which are found various absorption lines. These absorption lines are formed by vibrational or rotational transitions by molecules in the atmosphere. For example an absorption band in the thermal IR region centred at $15\mu\text{m}$ is a result of vibrational transition by CO_2 molecules and this absorption band is used for retrievals of atmospheric temperatures.

In general absorption lines are never sharp but are instead broadened by molecular collisions (called pressure or collisional broadening) and/or by Doppler broadening. In addition, the earth's surface and the atmosphere emit radiation that is determined by radiative characteristics of the emitting surfaces such as their temperature and emissivity. Often the emitted radiation is scattered and consequently it reaches the radiometer indirectly. So the measured radiance by a radiometer onboard a satellite originates from combined processes of emission, absorption and scattering of

radiation by the surface and the intervening atmospheric layers. The above processes that take place in the terrestrial atmosphere is described by a differential equation called the radiative transfer equation and it enables a quantitative computation of radiance at the top of the atmosphere. As these measured radiances depend directly on atmospheric temperature and concentrations of radiatively active gases (e.g. water vapour) we can by inverting the radiative transfer equation infer the vertical distribution of atmospheric temperature and/or concentrations of absorber gases.

In the 4DVAR analysis scheme used in ACCESS-G radiance measurements are directly assimilated using an observation operator which in the case of radiance measurements is the radiative transfer model described above. In 4DVAR an analysis is obtained by minimising the following cost function:

$$J(x_0) = \frac{1}{2}(x_0 - x^b)^T B^{-1}(x_0 - x^b) + \frac{1}{2} \sum_{i=1}^N [y_i - H_i(x_0)]^T R_i^{-1} [y_i - H_i(x_0)]$$

where x_0 is the state vector to be minimized, x^b is the model background from the previous cycle, y_i is a vector of observation values; B is the background error covariance matrix; R_i is the observation error covariance matrix; H_i is the nonlinear observation operator. The subscript i refers to times within the assimilation window at which observations are available (Kalnay, 2003; Daley, 1993).

As the size of the state vector x_0 is of the order 10^9 and that of the background error covariance matrix is therefore of the order 10^{18} the minimum of this cost function cannot be computed explicitly. To make the numerical solution of $J(x_0)$ computationally feasible, various approximations are made while retaining the essential atmospheric dynamics and some of the statistical properties. First $J(x_0)$ is recast into an incremental form (Courtier 1994); then a preconditioning step is applied to transform the state vector to a control vector in such a way that the background error covariance matrix in the control variable space becomes both a diagonal and an identity matrix (UK Met Office, 2006 and references therein). This preconditioning improves the condition number of the cost function and consequently a significant speed-up of the minimization is achieved.

In model space, the cost function $J(x_0)$ is applied to the prognostic variables of the state vector x_0 , that is temperature, humidity, etc. As the observation error covariance matrix R_i is assumed to be diagonal the multivariate relationship between different analysed variables is controlled by the background error covariance matrix B . Thus the role of IR and MW radiance measurements in data assimilation is to

<http://www.cawcr.gov.au/publications/researchletters.php>

constrain primarily the model's temperature and humidity fields both in space and time. Moreover because of the dynamic constraint built into B 4DVAR modifies other (unobserved) variables in a dynamically consistent way. Lastly the spatial correlation in B acts to spread observational information from well observed areas to data sparse areas.

Data Denial Experiment

In a data denial Observing System Experiment, one or more groups of observations are withheld from the assimilation in order to assess the impact they have on the resulting analysis and subsequent forecasts. In this study two assimilation and forecast runs were set up: a control run which closely matched the configuration used in operational APS1 ACCESS-G and which used identical observation types and quantity of observations; on the other hand, for the data-denial run all satellite observations were removed from assimilation leaving only the conventional, in-situ data.

Other than the difference in the satellite data usage the two runs used identical settings of OPS, VAR and UM. In addition to both runs being identical, same static-regression coefficients were used to bias-correct satellite radiances from the beginning of the experiment and then after two weeks of cycling the regression coefficients were independently updated.

In both runs the model resolution used was 0.563 deg longitude by 0.375 deg latitude and 70 levels (N320L70) with model top at 80 km. The resolution of the 4DVAR grid (i.e. the resolution of the Perturbation Forecast Model) was N144L70. The observations were assimilated in 6-hourly cycles with the 4DVAR assimilation window of 6 hours centred at 00, 06, 12 and 18 UTC.

The experimental period started from 26 October, 2011 12 UTC and ended on 30 October, 2011 18 UTC. During this period severe thunderstorms occurred in central and eastern parts of Victoria resulting in widespread heavy rainfall. This case was examined in more detail in the next section.

Results and Discussions

Figures 6 and 7 show the anomaly correlations for mean-sea level pressure forecasts from 2 runs: the control run which assimilated all available satellite data and the experimental run where all satellite observations were excluded globally. Figure 6 compares the verification scores between the 2 runs for the Northern Hemisphere and Figure 7 is for the Southern Hemisphere.

For the Northern Hemisphere (Figure 6) there is a

degradation of forecast skill of around 6-12 hours when no satellite data are used. However the impact in the Southern Hemisphere is striking: Figure 7 shows that satellite data on average gives 2.5 to 3 days of predictability in the Southern Hemisphere. The relatively minor role that the satellite observing system plays for the forecast quality in the Northern Hemisphere is due to the very extensive and high quality conventional observing network (see for example Figures 1 and 2). Consequently removal of satellite observations had a much smaller detrimental effect on the Northern Hemisphere predictability.

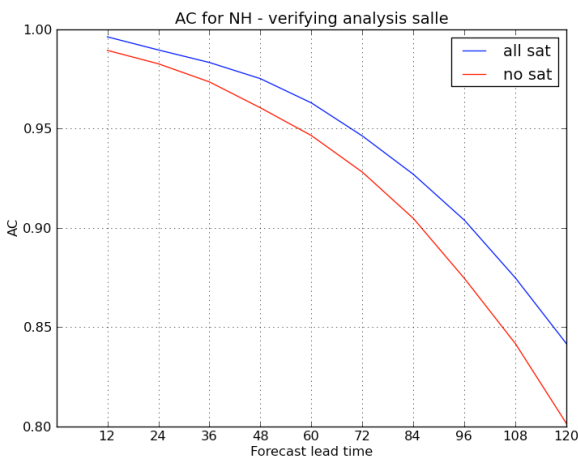


Figure 6 Anomaly correlations of mean sea-level pressure for the control run (blue) and the data-denial run (red) as a function of forecast lead times. The control analyses were used as verifying analyses. The verification scores were calculated for the Northern Hemisphere.

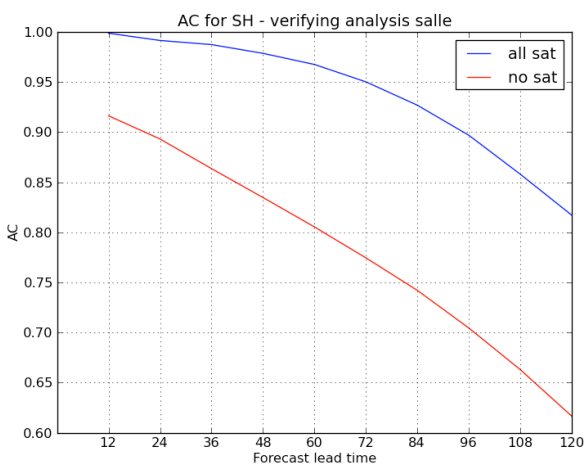


Figure 7 Same as for Figure 6, but for the Southern Hemisphere.

The anomaly correlation score shows broad-scale forecast quality and is a suitable measure for variables with smooth spatial variability. In order to assess the impact of removing satellite observations on a more tangible weather parameter the

quantitative precipitation forecasts (QPF) from the two runs were validated using a rainfall verification method described in Ebert and McBride (2000). It was applied to a severe thunderstorm event which took place in central and eastern Victoria over the 8th and 9th of November 2011. In Figure 8 the left map shows 24-hour accumulated rainfall forecast between 20111108 00 UTC and 20111109 00 UTC. The QPF forecasts were 48-hour and 72-hour forecasts based on 20111106 00 UTC control analysis. The map on the right shows validating gridded rainfall analysis, which used a network of rain gauges. As is apparent the general pattern of predicted rain follows the analysis with indications of heavy rainfall in central and eastern Victoria. Corresponding maps for the rainfall forecast from the data-denial run are shown in Figure 9. Although the general spatial pattern of rainfall seems reasonable the forecast fails to indicate any hint of widespread heavy rainfall. An objective categorical statistics comparing the 2 forecasts are shown in Table 2 where the QPF, which used satellite data shows improved scores over the forecast with only the conventional observations. This improvement is further demonstrated when the scores for the duration of the experiment are aggregated (Table 3). The results clearly show that satellite observations extend useful predictability of QPF.

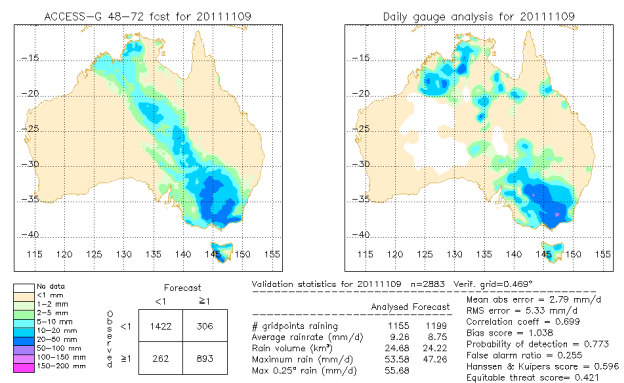


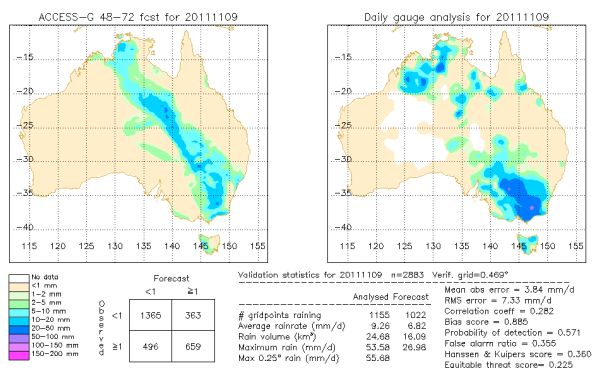
Figure 8 Rainfall verification for a widespread heavy rain case. QPF from control analysis based 20111106 00 UTC. Accumulated rainfall between +48 and +72 forecasts (left map). Validating gridded rainfall analysis is on the right map.

Table 2 A sample of categorical statistics for rainfall verification for the heavy rainfall case described in the text.

	Correlation Coefficient	Detection Probability	Hansen & Kuipers Score
All sat (control)	0.70	0.77	0.60
No sat (data denial)	0.28	0.57	0.36

Table 3 Aggregated rainfall verification scores for the period 20111101 to 20111130.

	Correlation Coefficient	Detection Probability	Hanssen & Kuipers Score
All sat (control)	0.41	0.73	0.51
No sat (data denial)	0.26	0.61	0.36

**Figure 9** Same as for Figure 8, but for data-denial run

Conclusions and Further Work

This study demonstrates quantitatively the importance of satellite observing system for the Bureau's current operational global ACCESS-G NWP forecasts. The gross verification scores were shown to demonstrate that the value of the satellite observing system for the Southern Hemisphere is equivalent to 2.5 to 3 days of predictability, a remarkable fact compared to the satellite impact in the Northern Hemisphere where it was estimated to be around 6 to 12 hours. A demonstration of what this may mean for day-to-day forecast guidance is illustrated by a single severe weather case study where the QPF field was objectively validated. Also shown was the aggregated QPF verification scores which further demonstrate the vital role satellite observations play in extending the predictability of a very tangible weather parameter such as rainfall. Overall the results confirm anecdotal evidence coming from operational forecasters who have given overwhelmingly positive feedback on the quality of ACCESS NWP guidance.

One of the shortcomings of any data-denial experiment is its computational expense and hence its inability to answer very detailed questions. For example, assessing impacts on forecasts of a single instrument or a single channel would be computationally prohibitive. An alternative but a powerful methodology is the forecast sensitivity to observations (FSO) using an adjoint model. Here an adjoint model is used to propagate an aspect of forecast error back to the analysis time and an

adjoint of data assimilation is then used to evaluate the impact of each individual observation or a group of observations. This work is well under way in CAWCR and we hope to publish the result in the near future.

Acknowledgements

Jin Lee thanks the scientific and IT support staff of CAWCR ESM Research Program for their invaluable assistance with running the ACCESS-G NWP system. He also thanks Jim Fraser for the permission to use NMOC's operational observation coverage plots.

References

- Bouttier, F. and Kelly, G. 2001: Observing-system experiments in the ECMWF 4D-Var data assimilation system. *Q. J. R. Meteorol. Soc.*, 127, 1469-1488.
- Courtier, P., Thepaut, J.-N. and Hollingsworth, A. 1994: A strategy for operational implementation of 4D-Var, using an incremental approach. *Q. J. R. Meteorol. Soc.*, 120, 1367-1388.
- Daley, R. 1993: *Atmospheric Data Analysis*. Cambridge University Press.
- Ebert, E. and McBride, J. 2000: Verification of precipitation in weather systems: Determination of systematic errors. *J. Hydrology*, 239, 179-202.
- Davies, T., Cullen, M. J. P., Malcolm, A. J., Mawson, M.H., Staniforth, A., White, A. A. and Wood, N. 2005: A new dynamical core for the Met Office's global and regional modelling of the atmosphere. *Q. J. R. Meteorol. Soc.*, 131, 1759-1782.
- Fraser, J. 2012: APS1 upgrade of the ACCESS-G Numerical Weather Prediction system. NMOC Operational Bulletin Number 93.
- Kalnay, E. 2003: *Atmospheric Modeling, Data Assimilation and Predictability*. Cambridge University Press.
- Kelly, G. and Thepaut, J.-N. 2007: Evaluation of the impact of the space component of the Global Observing System through Observing System Experiments. Seminar on recent developments in the use of satellite observations in numerical weather prediction, 3-7 September 2007. [Available online at <http://www.ecmwf.int/publications/library/ecpublicati ons/pdf/seminar/2007/Kelly.pdf>]
- Le Marshall, J., Xiao, Y., Norman, R., Zhang, K., Rea, A., Cucurull, L., Seecamp, R., Steinle, P., Puri, K., Fu, E. and Le, T. 2012: The application of radio occultation observations for climate monitoring and numerical weather prediction in the Australian region. *Australian Meteorological and Oceanographic Journal*, 62, 323-334.
- Milton, S. F. and Earnshaw, P. 2007: Evaluation of Surface Water and Energy Cycles in the Met Office Global NWP Model Using CEOP Data. *J. Meteorol. Soc. Japan*. 85A. 43-72.

Puri, K. *et al.* 2010: Preliminary results from Numerical Weather Prediction implementation of ACCESS. CAWCR Research Letters, 5, 15-22.

Rawlins F, Ballard S., Bovis K., Clayton A., Li D., Inverarity G., Lorenc A., Payne T. 2006. The Met Office global four-dimensional variational data assimilation scheme. Q. J. R. Meteorol. Soc., 133, 347–362.

UK Met Office, 2006: Control Variable Transforms. VAR Scientific Documentation paper 10. 11 pp.

Zapotocny T., Jung J., Le Marshall J. and Treadon, R. 2007. A Two-Season Impact Study of Satellite and In Situ Data in the NCEP Global Data Assimilation System. Wea. Forecasting, 22, 887-909

Vertical Structure and Diabatic Processes of the MJO

A Global Model Inter-comparison Project: preliminary results from the ACCESS model

Hongyan Zhu, H. Hendon, M. Dix, Z. Sun, G. Dietachmayer and K. Puri

The Centre for Australian Weather and Climate Research

Bureau of Meteorology, Melbourne, Australia

hzhu@bom.gov.au

Introduction

As a dominant sub-seasonal mode of tropical atmospheric variability, the Madden-Julian Oscillation (MJO; Madden 1971) exerts pronounced influences on global climate and weather systems (Lau and Waliser 2005; Zhang 2005), and represents a primary source of predictability on sub-seasonal time scales (e.g., Waliser 2005; Gottschalck et al. 2010).

Realistic simulation of the MJO using global climate models continues to be a challenge (e.g., Kim et al. 2009). Several studies have highlighted the great sensitivity of the simulation of the MJO to the details of convection parameterizations, thus suggesting that deficiencies in the representation of tropical convection may be the primary contributor to the poor simulations.

Moreover, several recent studies emphasized critical roles of diabatic heating associated with vertically tilted propagating mesoscale systems and synoptic-scale waves associated with the MJO (e.g. Khouider et al. 2011). While the physics and dynamics of mesoscale and synoptic scale convective organization are understood at a basic level (Houze 2004; Kiladis et al. 2009), the interactive processes between these multi scale waves and the MJO remains elusive. Meanwhile, there has been little success with the parameterization of organized convection associated with these multi-scale waves. Such scale interactions and the understanding and parameterization of the “organized convection problem” represents key elements of the motivation for the WCRP/WWRP-THORPEX Year of Tropical Convection (YOTC; Moncrieff et al. 2007; Waliser and Moncrieff 2008, and <http://www.ucar.edu/yotc>).

Given the central role of the diabatic heating in the physics of the MJO, and the desire to improve model capability to simulate the MJO, the GCSS model inter-comparisons project on the vertical structure and diabatic processes of MJO has been designed to explore how the MJO vertical heating structures are represented in current GCMs.

<http://www.cawcr.gov.au/publications/researchletters.php>

The objective of this project is to characterize, compare and evaluate the heating, moistening and momentum mixing processes associated with the MJO that are produced by our global weather and climate models, with a particular focus on their vertical structure. The goal is to improve our understanding of the role that convection, cloud, radiative and dynamic processes play in the development and evolution of the MJO in order to achieve better fidelity of the MJO in our global prediction models.

ACCESS model results were submitted to the inter-comparison experiment of twenty-year climate simulations. Model simulations use specified SSTs, which cover the periods from 1991 to 2010. We aim to characterize diabatic heating, moisture, and cloud structures of multi-scale convective systems within the MJO convection envelope during the MJO life cycle and elucidate key model deficiencies in depicting the MJO heating and associated cloud structures, and provide critical guidance for further improvement of ACCESS model parameterizations of physical processes.

Model Description

The UK Met Office Unified Model (UM7.8) with GA2.0 model physics is used in this study. The model horizontal resolution is $1.875^{\circ} \times 1.25^{\circ}$ and the integration time step is 1200s.

The model uses a modified mass flux scheme based on Gregory and Rowntree (1990). The convective diagnosis is based on an undiluted parcel ascent from the near surface. The convective diagnosis is used to determine whether convection is possible from the boundary layer and, if so, whether the convection is deep or shallow depending on the level of the cloud top. The mid-level convection scheme operates on any instabilities found in a column above the top of the deep/shallow convection or above the boundary layer in columns where the surface layer is stable.

For deep convection, the cloud-base mass-flux is

calculated based on the reduction to zero of Convectively Available Potential Energy (CAPE) over a given timescale. The CAPE closure has been modified in various ways to try to address model stability problems (grid point storms). W based CAPE closure is the option used in most model configurations. In this scheme, if the maximum large-scale vertical velocity, evaluated before convection, is larger than the threshold vertical velocity, the CAPE timescale is reduced to remove the convective instability faster. For deep convection, convective entrainment rates use prescribed profiles. Many recent studies have found that increasing the convective entrainment rates will improve MJO simulation in the model, therefore in this work the mixing entrainment rates in the convection parameterization scheme are increased by 1.5. Mixing detrainment rates depend on relative humidity and an adapted detrainment scheme is used to calculate the forced detrainment rates. The representation of Convective momentum transports (CMT) is based on an eddy viscosity model and a flux gradient approach has been introduced in the latest version of model.

The model uses the prognostic cloud fraction and prognostic condensate (PC2) scheme of Wilson et al. 2008. For the boundary layer scheme, turbulent fluxes of heat, moisture and horizontal momentum in the boundary layer are represented by a first-order K -profile closure as described by Lock et al. (2000). The model radiation scheme uses the modified version of Edwards and Slingo (1996) scheme based on rigorous solution of the two-stream scattering equations including partial cloud cover.

Results and Discussion

MJO simulation

To demonstrate the ability of the model to simulate eastward propagating intraseasonal variability, in Figure 1, we calculated the lead-lag correlation coefficients between 20-100 days bandpass filtered data using the central Indian Ocean regional time series and the associated near-equatorial data at all longitudes to produce a time-longitude plot of correlation values, and then average the diagrams from all years together and apply 1% significance level.

The observation 850 hPa wind is from the NCEP analysis. The 850 hPa zonal wind analysis of Figure 1 exhibits eastward propagation during boreal winter with a further eastward extension of significant anomalies to around 180°E longitude, and compared to the observations, the model exhibits coherent eastward propagation across Indian Ocean and West Pacific Ocean.

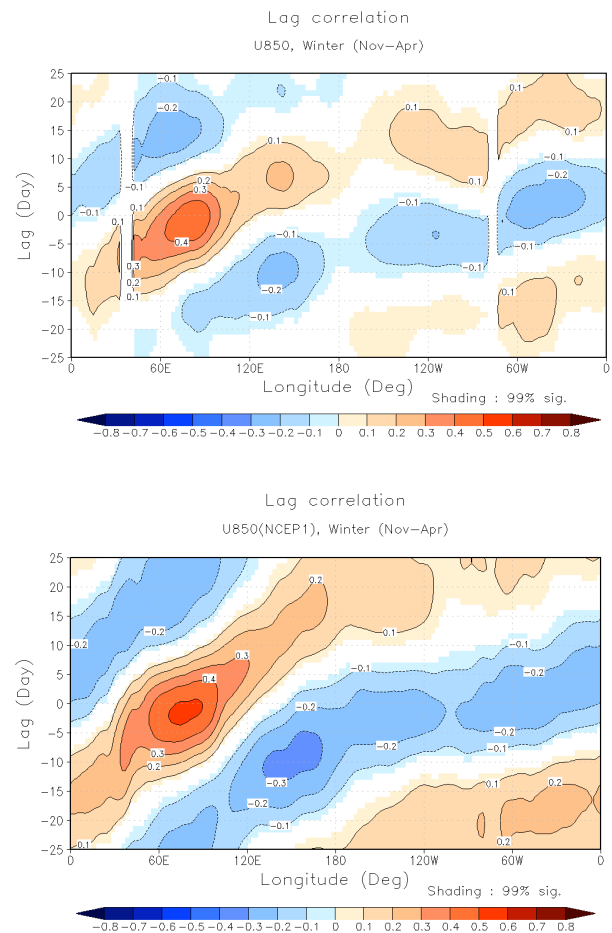


Figure 1 Lag correlations between near-equatorial U850 and 20-100 day filtered U850 in the Indian Ocean region.

One school of thought maintains that MJO dynamics are regulated by a recharge-discharge mechanism. Various studies have showed that shallow convection and its associated shallow vertical circulation help to moisten the atmosphere column. In this work, we will compare the moisture budget from model large-scale dynamics and parameterized convection to see whether model is able to simulate this discharge and recharge associated with deep circulation and investigate what is the main contributor to this mechanism.

Vertical moisture budget

In the moisture budget equation below, the underlined term represents the large-scale advection, including both horizontal and vertical advection. Q represents the contribution from the parameterized model physics. For the troposphere, this contribution mainly comes from the convection parameterization scheme.

$$\frac{\partial q}{\partial t} = -\left(\underline{u \frac{\partial q}{\partial x} + v \frac{\partial q}{\partial y}}\right) - w \left(\frac{\partial q}{\partial z}\right) + Q$$

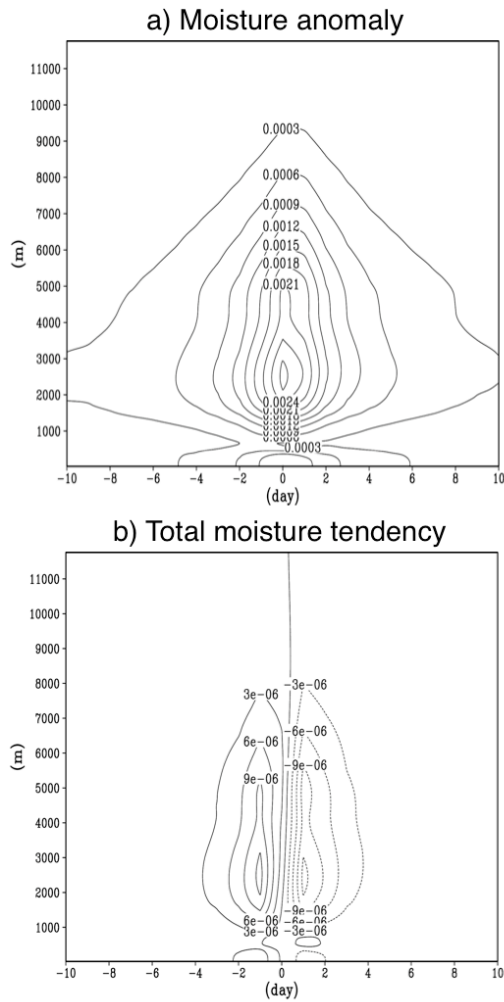


Figure 2 Moisture budget relative to intense rainfall events (60E-180E, 20S-equator) for (a) moisture anomaly (kg kg^{-1}) and (b) total moisture tendency (10^{-3} s^{-1}).

Figure 2a shows the moisture anomaly relative to the intense rainfall events. The intensive rainfall events are defined that the rainfall rates are bigger than one standard deviation, which is 9.6 mm/day. The moisture starts to build up before the intense rainfall and release after the intense rainfall above the boundary layer. Consistent with the moisture anomaly, the total moisture tendency is positive before the intense rainfall and negative after the intense rainfall. Total moisture tendency is asymmetric relative to the maximum precipitation, corresponding to the recharge and discharge process of organized convection in the Tropics. The moistening and drying are roughly symmetric relative to day zero. Figure 3a shows the lag relationship of large-scale moisture advection according to the peak time of intense rainfall events. Large-scale moisture advection moistens the troposphere during the intense rainfall. There is clear asymmetric structure relative to the maximum rainfall.

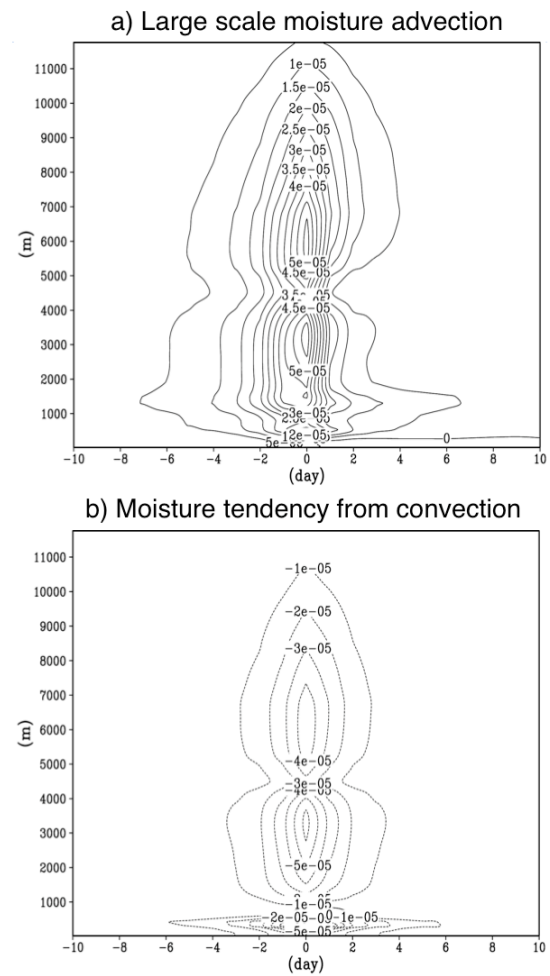


Figure 3 Moisture budget relative to intense rainfall events for (a) large-scale moisture advection (10^{-3} s^{-1}) and (b) moisture tendency from convection (10^{-3} s^{-1}).

The moisture builds up 6 days ahead of the maximum rainfall, and stops two days after the maximum rainfall. Parameterized convection tends to dry the troposphere mainly due to compensating subsidence. The drying is fairly symmetric relative to the maximum rainfall, occurring between -6 and +6 days.

As seen in the moisture budget equation, the large-scale moisture advection has two parts, horizontal and vertical advection. Figure 4a is the vertical moisture advection relative to the intense rainfall events. The large-scale vertical advection moistens the troposphere due to the vertical transport of moisture. This moistening is symmetric relative to the maximum rainfall, and approximately balanced by the drying effects of the parameterized convection. Figure 4b shows the horizontal moisture advection relative to the intense rainfall events. Horizontal moisture advection has an asymmetric structure relative to the intense rainfall events. There is positive moisture advection that starts four

- pre-moistening by shallow convection before the intense rainfall.
4. Model recharge of moisture is the result of horizontal moisture convergence.
 5. Moisture advection between the equator and polewards latitudes after the intense rainfall events leads to the discharge of moisture.

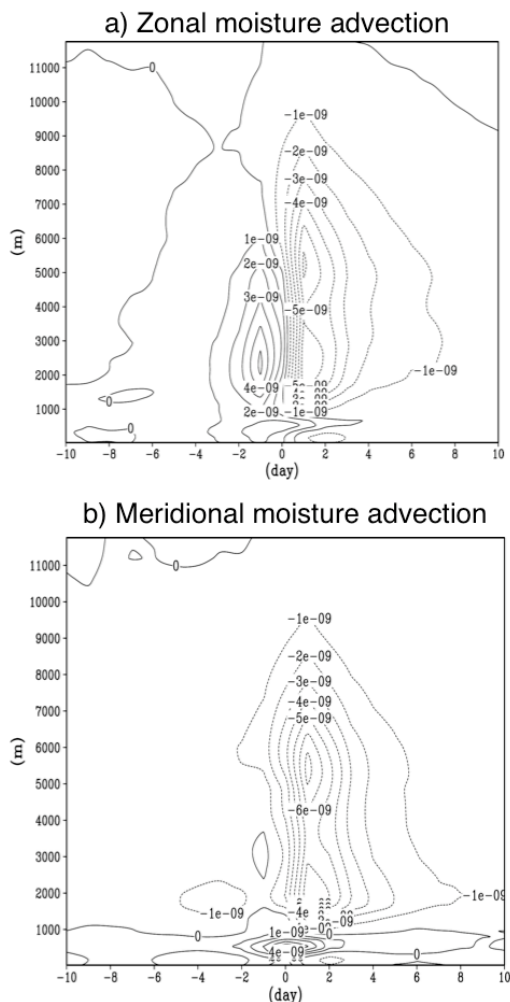


Figure 5 Moisture budget for the southern hemisphere relative to intense rainfall events for large-scale (a) zonal moisture advection (s^{-1}) and (b) meridional moisture advection (s^{-1}).

Acknowledgements

This work was supported by the Australian Climate Change Science Program, as part of the “ACCESS Coupled Climate Model Development” project.

References

Edwards, J.M. and Slingo, A., 1996: Studies with a flexible new radiation code. 1: Choosing a configuration for a large-scale model. *Quart. J. Royal Meteorol. Soc.*, 122, 689-719.

Gottschalck, J., M. Wheeler, K. Weickmann, F. Vitart, N. Savage, H. Lin, H. Hendon, D. Waliser, K. Sperber, M. Nakagawa, C. Prestrelo, M. Flatau, and W. Higgins, 2010: A Framework for Assessing Operational Madden-Julian Oscillation Forecasts: A CLIVAR MJO Working Group Project, *Bull. Amer. Meteor. Soc.*, 91, 1247-1258.

Houze, R. A., Jr., 2004: Mesoscale convective systems. *Rev. Geophys.*, 42, 10.1029/2004RG000150, 43 pp.

Kim, D., K. Sperber, W. Stern, D. Waliser, I.-S. Kang, E. Maloney, S. Schubert, W. Wang, K. Weickmann, J. Benedict, M. Khairoutdinov, M.-I. Lee, R. Neale, M. Suarez, K. Thayer-Calder, and G. Zhang. 2009: Application of MJO Simulation Diagnostics to Climate Models, *J. Climate*, 22, 6413-6436.

Khouider, B., A. St-Cyr, A. J. Majda, and J. Tribbia, 2011: MJO and convectively coupled waves in a coarse resolution GCM with a simple multcloud parameterization. *J. Atmos. Sci.*, 68, 240-264.

Kiladis, G. N., M. C. Wheeler, P. T. Haertel, K. H. Straub, and P. E. Roundy, 2009: Convectively coupled equatorial waves. *Rev. Geophys.*, 47, RG2003, doi:10.1029/2008RG000266.

Madden R. and P. Julian, 1971: Detection of a 40-50 day oscillation in the zonal wind in the tropical Pacific, *J. Atmos. Sci.*, 28, 702-708. Madden R. and P. Julian, 1994: Observations of the 40-50 day tropical oscillation: A review. *Mon. Wea. Rev.*, 112-814-837.

Moncrieff, M.W., M. Shapiro, J. Slingo, and F. Molteni, 2007: Collaborative research at the intersection of weather and climate. *WMO Bulletin*, 56, 204-211.

Lock, A.P., Brown, A.R., Bush, M.R., Martin, G.M. and Smith, R.N.B. (2000) A new boundary layer scheme for the Uni_ed Model. Part I: Scheme description and single column model tests. *Mon. Weather Rev.*, 128, 3187-3199.

Waliser, D., 2005: Predictability and forecasting. In: W.K.M. Lau and D.E. Waliser (Eds.), *Intraseasonal Variability in the Atmosphere-Ocean Climate System*. Praxis, Springer Berlin Heidelberg, 389-423.

Waliser, D.E., M.W. Moncrieff, 2008: Year of Tropical Convection (YOTC) Science Plan, WMO/TD-No. 1452, WCRP -130, WWRP/THORPEX- No 9, 26 pp.

Zhang, C. 2005: Madden-Julian Oscillation. *Reviews of Geophysics*, 43, 1-36.